Cytoskeletal activation of NHE1 regulates cell volume and DNA methylation

Qin Ni,[1,2,†] Zhuoxu Ge,[1,2,†] Yizeng Li,[3], Gabriel Shatkin[4], Jinyu Fu,[1,5], Kaustav Bera,[1,6], Yuhang Yang[7], Yichen Wang [2], Anindya Sen[1,6], Yufei Wu[1,2], Ana Carina Nogueira Vasconcelosi,[1,2], Andrew P. Feinberg[4,7,8], Konstantinos Konstantopoulos,[1,4,7,8] Sean X. Sun [1,2,*]

[1]Institute for NanoBioTechnology, Johns Hopkins University, Baltimore, MD, USA
[2]Department of Mechanical Engineering, Johns Hopkins University, Baltimore, MD, USA
[3]Department of Biomedical Engineering, Binghamton University, Binghamton, NY, USA
[4]Department of Biomedical Engineering, Johns Hopkins University, Baltimore, MD, USA
[5]Department of Physics, Johns Hopkins University, Baltimore, MD, USA
[6]Department of Chemical and Biomolecular Engineering,
Johns Hopkins University, Baltimore, MD, USA
[7]Department of Oncology, The Sidney Kimmel Comprehensive Cancer Center,
Johns Hopkins University School of Medicine, Baltimore, USA
[8]Center for Epigenetics, Johns Hopkins University School of Medicine, Baltimore, MD, USA
[†]These authors contribute equally

[*]To whom correspondence should be addressed; E-mail: ssun@jhu.edu.

The regulation of mammalian cell volume is crucial for maintaining key cellular processes. Cells can rapidly respond to osmotic and hydrostatic pressure imbalances during environmental challenges, generating fluxes of water and ions that alter volume within minutes. While the role of ion pump and leak in cell volume regulation has been well-established, the role of the actomyosin cytoskeleton and its substantial interplay with ion transporters are still unclear.

In this work, we discover a system of cell volume regulation controlled by cytoskeletal activation of ion transporters. Under hypotonic shock, NIH-3T3 and MCF-10A display a 20% secondary volume increase (SVI) following the initial regulatory volume decrease. We show that SVI is initiated by Ca^{2+} influx through stretch activated channel Piezo1 and subsequent actomyosin remodeling. Rather than contracting cells, actomyosin triggers cell swelling by activating Na^{+}-H^{+} exchanger 1 (NHE1) through their co-binding partner ezrin. Cytoskeletal activation of NHE1 can be similarly triggered by mechanical stretch and attenuated by soft substrates. This mechanism is absent in certain cancer cell lines such as HT1080 and MDA-MB-231, where volume regulation is dominated by intrinsic response of ion transporters. Moreover, cytoskeletal activation of NHE1 during SVI induces nuclear deformation, leading to DNA demethylation and a significant, immediate transcriptomic response in 3T3 cells, a phenomenon that is absent in HT1080 cells. Overall, our findings reveal the central role of Ca^{2+} and actomyosin-mediated mechanosensation in the regulation of ion transport, cell volume, DNA methylation, and transcriptomics.

1 Introduction

Cell size is a critical global variable that influences numerous essential cellular processes. Cells can sense and change their size during the cell cycle, and the failure of cell size control is an indicator of disease (*1, 2*). At minimum, the cell volume, which represents the 3-dimensional cell size, influences intracellular biochemical reactions by affecting concentrations of all cytoplasmic components. During interphase, the cell volume steadily increases due to the synthesis of new cytoplasmic proteins (*3*). On the other hand, mitotic cells can swell and increase their

volume by 10-20% in minutes without producing extra mass (*4, 5*). Moreover, short timescale cell volume changes can generate mechanical forces for cell rounding (*4, 6*), provide space for chromosome segregation (*7*), and also impact cell migration (*8–11*).

At the timescale of minutes, cell volume changes are predominantly due to water flux across the cell membrane, driven by both osmotic pressure and the hydraulic pressure gradients (*10, 12, 13*). When the cell size and shape are steady, any hydraulic pressure gradient is mechanically balanced by tension in the cell membrane and the actomyosin cortex (*14*). As a consequence, cell volume is sensitive to both environmental physical and chemical variables, including extracellular osmolarity (*1, 10, 15, 16*), media viscosity (*11, 17*), substrate stiffness or geometry (*18–21*), hydraulic resistance (*11, 22, 23*), and confinement (*24*).

To maintain the necessary balance between the osmotic pressure and the hydraulic pressure, cells use transmembrane ion fluxes to change the cytoplasmic solute concentration. Ion "pump and leak" has been identified as a major mechanism in volume regulation (*1, 25*), involving Na^+ and K^+ fluxes through ion pumps, exchangers and channels such as sodium-potassium ATPases (NKA) and sodium-hydrogen exchanger (NHE). The latter has been shown to be involved in mitotic swelling and cell migration (*5, 8, 11*). Actomyosin contractile force has been proposed as another way to control cell volume (*6, 12, 26, 27*). However, direct evidence showing volume regulation by actomyosin is lacking. A central question that arises is **whether actomyosin directly influences cell volume via contractile force or indirectly regulates cell volume via signals to ion transporters.** Ca^{2+} related signaling cascades initiated by mechanosensitive ion channels is a promising candidate that bridge actomyosin contractility with ion transport (*1, 28–30*). Currently, how cell volume regulation is achieved through actomyosin and Ca^{2+} mediated signaling is unknown.

In this work, we investigate the interplay between actomyosin dynamics, Ca^{2+} signaling, and ion fluxes in regulating cell volume. Our findings reveal that cells can maintain relatively

constant volume upon the inhibition of several crucial ion transporters or disruption of the actomyosin network, but display distinct volume adaptation dynamics under hypotonic stress. We identify a secondary volume increase (SVI) in NIH-3T3 fibroblasts and non-tumorigenic breast MCF-10A cells after the initial regulatory volume decrease, triggered by cytoskeletal activation of NHE1 via Ca^{2+} influx through the mechanosensitive channel Piezo1, actomyosin remodeling, and the NHE1-actin binding partner ezrin. The cytoskeletal activation of NHE1 is also validated by direct mechanical stretching of cells. This mechanism appears to be mostly absent in certain cancer cell types such as HT1080 fibrosarcoma and MDA-MB-231 metastatic breast cancer cells, or 3T3 cells grown on compliant substrates. Additionally, we reveal that SVI leads to large-scale chromosome modification, a strong reduction in DNA methylation, and significant changes in gene expression, signifying a novel mechanosensitive mechanism of cell adaptation to environmental challenges.

2 Results

2.1 Cell volume homeostasis and non-monotonic response to hypotonic shock

We first disrupted actomyosin network and inhibited ion transporters to examine cell volume changes using the fluorescence exclusion method (FXm) (*31, 32*) (Fig. 1a). We chose NIH-3T3 and HT1080 as two model systems to contrast cell-type specific behavior. Cells were seeded into the microfluidic FXm chambers at least one hour before imaging to allow for cell attachment and spreading. Media with various inhibitors were then flown into the chamber and cell volume was monitored for 1-4 hours after adding inhibitors by tracking single cells. We found that after disassembling the actin network via Latranculin A (LatA), stalling non-muscle myosin II via para-nitro-blebbistatin (n-Bleb), blocking actin-membrane binding partner ezrin via NSC668394 (NSC), and inhibiting upstream regulator Calmodulin (CaM) via W7, cell vol-

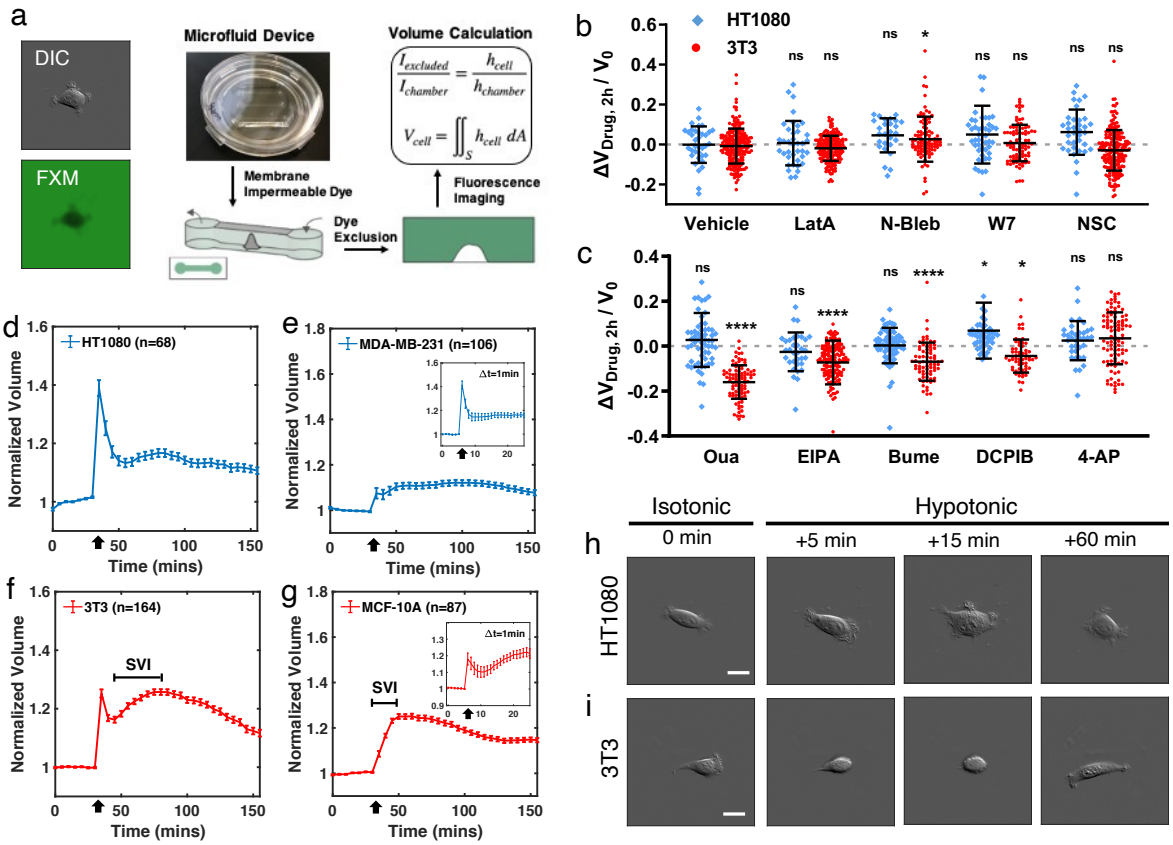

Figure 1: **Cell volume dynamics during inhibitions of ion transporters, disruption of cytoskeleton, and hypotonic shock.** (a) The schematic of the Fluorescence Exclusion method (FXm), and representative snapshots. (b) Fractional cell volume changes under vehicle control (0.5%DMSO) and drugs for cytoskeleton: Latrunculin A (LatA, diassemble actin network), para-nitro-blebbistatin (n-Bleb, Myosin II inhibitor), W7 (blocking Calmodulin - Ca^{2+} binding), and NSC668394 (NSC, blocking ezrin-actin binding). (c) Fractional cell volume change when exposed to ion transporter inhibitors: Ouabain (Oua, NKA inhibitor), EIPA (NHE inhibitor), Bumentanide (Bume, NCKK inhibitor), DCPIB (VRAC inhibitor), and 4-AP (VGKC inhibitor). (b, c) Cell volume were tracked 1-4 hours until fully adapted (see methods for details). (d-g) Cell volume of HT1080 (d), MDA-MB-231 (e), NIH-3T3 (f), Mcf-10a (g) before and after hypotonic shock. Hypotonic solutions were injected into FXm channels at 30 mins. Inserts in (e,g) are volume imaged at 1 min frame rate for MDA-MB-231 (n=35) and MCF-10A (n=29), respectively. (h-i) Representative DIC images of 3T3 (h) and HT1080 (i) before and 5, 15, and 60 min after hypotonic shock. (b,c) Error bars indicate standard deviation, and Kruskal–Wallis tests followed by Dunn's multiple-comparison test were conducted between data sets and the vehicle control of the corresponding cell type. ****p<0.0001, ***p<0.001, **p<0.01, and ns p>0.05. (b) $n^{HT1080}_{Vehicle} = 36, n^{3T3}_{Vehicle} = 213, n^{HT1080}_{LatA} = 190, n^{3T3}_{LatA} = 38, n^{HT1080}_{n-Bleb} = 27, n^{3T3}_{n-Bleb} = 102, n^{HT1080}_{W7} = 46, n^{3T3}_{W7} = 89, n^{HT1080}_{NSC} = 36, n^{3T3}_{NSC} = 202$. (c) $n^{HT1080}_{Oua} = 60, n^{3T3}_{Oua} = 94, n^{HT1080}_{EIPA} = 33, n^{3T3}_{EIPA} = 147, n^{HT1080}_{Bume} = 61, n^{3T3}_{Bume} = 76, n^{HT1080}_{DCPIB} = 47, n^{3T3}_{DCPIB} = 62, n^{HT1080}_{4-AP} = 36, n^{3T3}_{4-AP} = 100$. (d-g) Error bars represent the standard error of mean (SEM). Black arrows indicate the time of osmotic shock. (h, i) Scale bars, 20 µm.

ume changes were less than 10% on average (Fig. 1b). We also performed pharmacological inhibition on ion transporters with significant expression in 3T3 and HT1080 (measured by RNAseq: Supplementary Text-1) and that are known as cell volume regulators (*1*): NKA (inhibited by Ouabain), NHE (inhibited via EIPA), Na^+-K^+-Cl^- cotransporter (NKCC, inhibited via bumentide), volume-regulated anion channel (VRAC, inhibited via DCPIB), and voltage-gated K^+ channel (VGAC, inhibited via 4-Aminopyridine). Both HT1080 and 3T3 volumes changed less than 10%, with an exception being the $\sim$20% volume decrease in 3T3 treated with Ouabain (Oua) (Fig. 1c). Interestingly, cell volume change displayed significant cell to cell variation, and 3T3 volume decreased while HT1080 volume increased under DCPIB, Oua, and NSC treatment.

We next perturbed cell volume by applying 50% hypotonic shock and examined the subsequent cell volume dynamics. HT1080 cells underwent monotonic regulatory volume decrease within 20 minutes after hypotonic shock, reaching a steady state that is 10% higher than its isotonic volume (Fig. 1d). Similar monotonic regulatory volume decrease with a faster recovery speed was found in MDA-MB-231 (Fig. 1e) and also recently reported for Hela Kyoto cells (*15, 16*). Hypotonic stress also resulted in a slight increase in cell base area without significant cell shape change (Fig. 1i, Fig. S1b, and Video 1). In 3T3 cells, volumes recovered to $\sim$18% higher than its isotonic volume after 10 minutes of hypotonic shock (Fig. 1f), accompanied with $\sim$ 30% base-area reduction (Fig. S1a) and significant cell rounding (Fig. 1h, Fig. S1b, and Video 2). Surprisingly, 3T3 displayed a second phase of volume increase after the initial regulatory volume recovery, followed by another phase of volume decrease. (Fig. 1f). The secondary volume increase (SVI) was also found in MCF-10A (Fig. 1g), indicating that the SVI is not a 3T3 specific response. Tracking single cell volume trajectories revealed significant cell to cell variations, and both SVI and the monotonic volume recovery dynamics were found in all four cell lines examined (Fig. S1d-e). Majority of 3T3 and MCF-10A displayed the SVI

phenotype with varying timescales (on average 45 mins for 3T3 and 42 mins for MCF-10A, Fig. S1f) and magnitudes (on average 18% for 3T3 and 30% for MCF-10A, Fig. S1g). Since the doubling time of these cell lines is $\sim$ 15-17 hours (Fig. S1h), SVI is not a consequence of cell growth. On the other hand, 50% hypertonic shocks resulted in rapid cell volume decrease without significant regulatory volume increase in both 3T3 and HT1080 (Fig. S1i-j).

2.2 Hypotonic shock triggers cell volume regulation via NKA and NHE

Na^+-K^+ pump and leak are known as a major contributor to cell volume regulation (*1, 25*), thus we investigated how Na^+-K^+ transporters regulate cell volume after applying hypotonic shock. We first examined NKA, which regulates cell volume decrease by importing 2 K^+ and exporting 3 Na^+ (*33*), using its inhibitor Oua. Cells were subjected to inhibitors as described above before applying osmotic shock. Upon high dosage (250μM) of Oua treatment, HT1080's initial cell volume peak (defined as the first measured time point after hypotonic shock) reached 60% higher than its isotonic volume, and the volume continuously increased over the next 2 hours (Fig. 2a, c), leading to significant cell swelling (Fig. 2c and i, Video 3). Similar results were observed in MDA-MB-231 and MCF-10A (Fig. S2a, b), confirming that NKA is a major contributor to regulatory volume decrease. Blocking NKA also increased the initial cell volume peak of 3T3 cells, however, their volume still recovered (Fig. 2b, d). These markedly different behaviors suggests completely different cell volume regulatory mechanisms exist in tissue cells.

We next examined NHE, whose activation leads to an increase of both cell volume and pH by importing Na^+ and exporting H^+ (*34–36*). HT1080 and MDA-MB-231 treated with NHE inhibitor EIPA displayed a significantly faster volume recovery (Fig. 2e, and Fig. S2c), indicating that NHE rapidly acts against the regulatory volume decrease triggered by hypotonic shock. 3T3 and MCF-10A treated with EIPA showed a decrease of the initial peak as well as complete removal of SVI (Fig. 2f and Fig. S2d). Specifically, we found that the removal

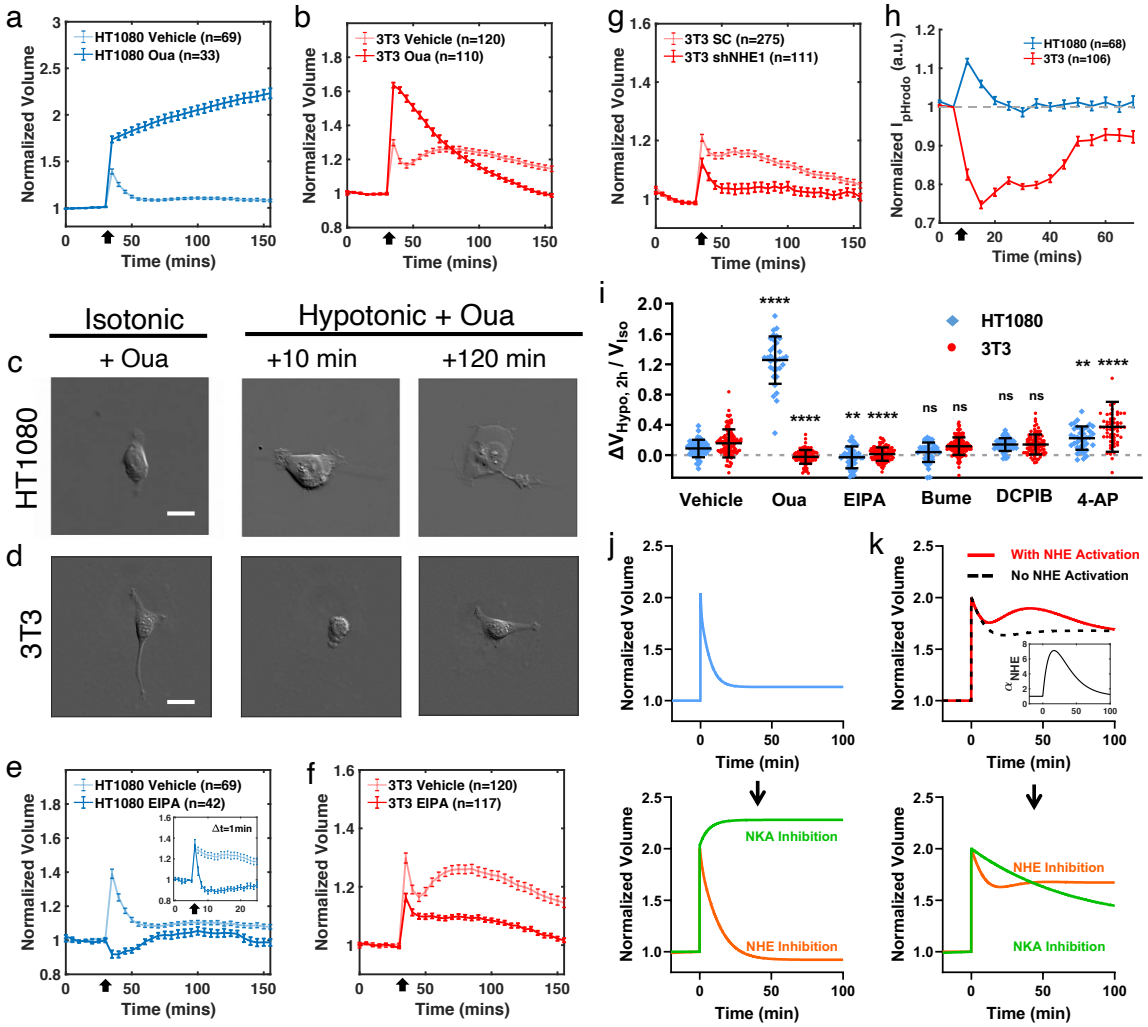

Figure 2: **Ion pump and leaks regulates cell volume after hypotonic shock.** (a, b) 3T3 (a) and HT1080 (b) volume under Oua treatment and hypotonic shock. (c, d) Representative DIC images of HT1080 (c) and 3T3 (d) before, 10 min, and 120 min after hypotonic under Oua treatment. (e) HT1080 volume dynamics under EIPA treatment. Insert has 1 min frame rate (Vehicle n = 53, EIPA n = 25). (f) 3T3 volume dynamics under EIPA treatment. (g) 3T3 scramble control (SC) and shNHE1 volume dynamics. (h) Intensity of pHrodo-red AM for HT1080 and 3T3. Hypotonic shock was applied at 5 mins. An increase in pHrodo-red intensity indicates decrease in pH. (i) Relative cell volume change 2 hours after applying hypotonic shock under drug inhibition of ion channels and transporters. (j, k) Computer simulation of HT1080 (j) and 3T3 (k) with hypotonic shock and inhibition of NKA and NHE. Insert in (k) indicates the NHE activation function, where α_{NHE} is the permeability coefficient of NHE. See supplementary information for model details. (a,b, e-h) Error bars indicate the SEM. (i) Error bars indicate standard deviation. Kruskal–Wallis tests followed by Dunn's multiple-comparison test were conducted between data sets and the vehicle control of the corresponding cell type. $\mathrm{n}^{\mathrm{HT1080}}_{\mathrm{Vehicle}} = 69, \mathrm{n}^{\mathrm{3T3}}_{\mathrm{Vehicle}} = 120, \mathrm{n}^{\mathrm{HT1080}}_{\mathrm{Oua}} = 33, \mathrm{n}^{\mathrm{3T3}}_{\mathrm{Oua}} = 110, \mathrm{n}^{\mathrm{HT1080}}_{\mathrm{EIPA}} = 42, \mathrm{n}^{\mathrm{3T3}}_{\mathrm{EIPA}} = 117, \mathrm{n}^{\mathrm{HT1080}}_{\mathrm{Bume}} = 39, \mathrm{n}^{\mathrm{3T3}}_{\mathrm{Bume}} = 136, \mathrm{n}^{\mathrm{HT1080}}_{\mathrm{DCPIB}} = 47, \mathrm{n}^{\mathrm{3T3}}_{\mathrm{DCPIB}} = 88, \mathrm{n}^{\mathrm{HT1080}}_{\mathrm{4-AP}} = 37, \mathrm{n}^{\mathrm{3T3}}_{\mathrm{4-AP}} = 54$. (c, d) Scale bars, 20 µm.

of SVI was controlled by NHE isoform 1 (NHE1) as confirmed by NHE1 knockdown using RNA interference (shNHE1, Fig. 2g and Fig. S2f), and the selective NHE1 inhibitor Bix (Fig. S2e). We then used an intracellular pH indicator, pHrodo Red-AM, to further examine the NHE activity. Upon hypotonic shock, 3T3 displayed a significantly higher intracellular pH that slowly recovered over 40 minutes, in striking contrast to the immediate decrease and rapid pH recovery found in HT1080 (Fig. 2h). These results confirm that NHE1 is activated after hypotonic shock and its activity is sustained during SVI in 3T3, whereas NHE1 activation in HT1080 is transient. Overall, our observations indicate that NHE1 is another major cell volume regulator, and the observed SVI is associated with NHE1 activity.

We also examined the effects of other major ion transporters in volume recovery after hypotonic shock. Inhibition of NKCC (Fig. S2g-h) or VRAC (Fig. S2i-j) slightly raised the initial volume peak, while blocking passive VGKC significantly increased the steady state volume after hypotonic shock (Fig. 2i, Fig. S2k-i). However, none of these inhibitors changed the features of the monotonic recovery in HT1080 and the SVI in 3T3.

2.3 Theoretical modeling explains cell type specific volume regulatory behavior

To probe potential mechanisms underlying the distinct cell volume regulation of 3T3 and HT1080, we used a computational model of cell volume regulation that considers fluxes from commonly expressed ion transporters, H+ and HCO_3^-, and membrane electrical potential (Fig. S2m). In the model, the cell volume is modulated by osmotic and hydrostatic pressure gradients, and ion fluxes are determined by the activities of ion transporters (related to regulation of channel opening and their expression levels) as well as the chemical and mechano-physiological states such as cell cortical tension, pH, and membrane potential. Model details can be found in Supplementary Text-2. HT1080 and 3T3 cells display distinctly different volume adaptation dy-

namics, both at very short time scales immediately after osmotic change, and also at longer time scales over several minutes. Therefore, we looked for different parameter regimes in the model that can produce similar distinct behavior. Using an unbiased search of activity coefficients of ion transporters and conducting a principal component analysis (PCA), we indeed found two regions in parameter space that corresponds to the types of cell volume regulation behavior observed in HT1080/MDA-MB-231 and 3T3/MCF-10A (Supplementary Text-3). PCA analysis confirmed that NHE and NKA are two key regulators in initial regulatory volume decrease, in agreement with the experimental observation. The two sets of parameters also correctly predicts the slightly higher homeostatic cytoplasmic pH observed in HT1080 versus 3T3 (Fig. S2o). On the other hand, experimental data suggest that NHE activation at longer time scales of tens of minutes generates SVI in 3T3. Our modeling results show that such complex secondary volume dynamics can only be achieved with additional NHE activation (Fig. 2k). By incorporating a second phase of NHE activation into its activity coefficient, the model can generate the same type of volume increase as the SVI in 3T3 (Fig. S2n). These findings raise the question of how this activation is regulated in different cell types, and what is the purpose of SVI.

2.4 Actomyosin dynamics regulates SVI

Hypotonic shock not only alters intracellular osmolarity, but also exert forces on the actomyosin network and the cell membrane by expanding the cell surface (*12*). As a consequence, hypotonic stress has been reported to increase cell membrane tension (*15*) and lead to actin network reorganization (*37*). Thus, we examined the F-actin dynamics after hypotonic shock in 3T3 and HT1080 with EGFP-F-tractin. Confocal microscopy showed that in 3T3 cells, F-actin remodeled rapidly and formed a rounded actin cortex after osmotic shock (Fig. 3a), accompanied with elevated membrane tension (Fig. 3e, measured by membrane tension probe Flipper-TR and Fluorescence Lifetime Imaging Microscopy). The cortex reorganization and high mem-

brane tension were sustained during SVI. Quantitative immunofluorescence of phosphorylated myosin light chain (pMLC) also showed that 3T3 pMLC content increased after hypotonic shock and recovered after 60 minutes (Fig. S3a). In contrast, hypotonic stress did not trigger actin network remodeling in HT1080 (Fig. 3b) and there were no significant changes in the cell pMLC content (Fig. S3b). These observations suggest that 3T3 and HT1080 have distinct involvement of actomyosin machinery when responding to hypotonic stress, and we hypothesize that such difference is related to their distinct volume dynamics.

We then examined whether the observed actomyosin remodeling influences cell volume. Addition of LatA disassembled the actin network and halted its remodeling after hypotonic shock in 3T3 (Fig. 3c). LatA or another actin depolymerizer Cytochalasin D (CytoD) had limited impact on the initial recovery of 3T3 (Fig. 3f and Fig. S3c), while n-Bleb reduced the initial peak (Fig. S4b). Interestingly, all three drugs removed SVI in 3T3. LatA also removed SVI in MCF-10A (Fig. S3e). On the other hand, HT1080 treated with LatA still showed limited actin remodeling (Fig. S4a), and all three drugs did not significantly affect monotonic volume recovery compared to untreated cells (Fig. 3g, Fig. S3d, and Fig. S4c). Disrupting actin networks also decreased the steady state volume after hypotonic shock in 3T3 but not in HT1080 (Fig. S4d).

Substrate stiffness is known to alter F-actin network structure and change cytoskeletal forces (*38–41*). To further validate the role of actomyosin in SVI, we cultured 3T3 cells on PDMS substrates with varying stiffness and examine cell volume dynamics under hypotonic shock. As expected, 3T3 displayed a monotonic regulatory volume decrease on soft substrate at 3 and 15 kPa, in contrast to the observed SVI on 130 kPa substrate and on glass (Fig. 3h). In addition, hypotonic shock lead to a transient pH reduction and attenuated membrane tension for 3T3 cells grown on 15 kPa substrate (Fig. 3i). On the other hand, HT1080 displayed consistent monotonic volume regulatory decrease regardless of substrate stiffness (Fig. S4e). Collectively,

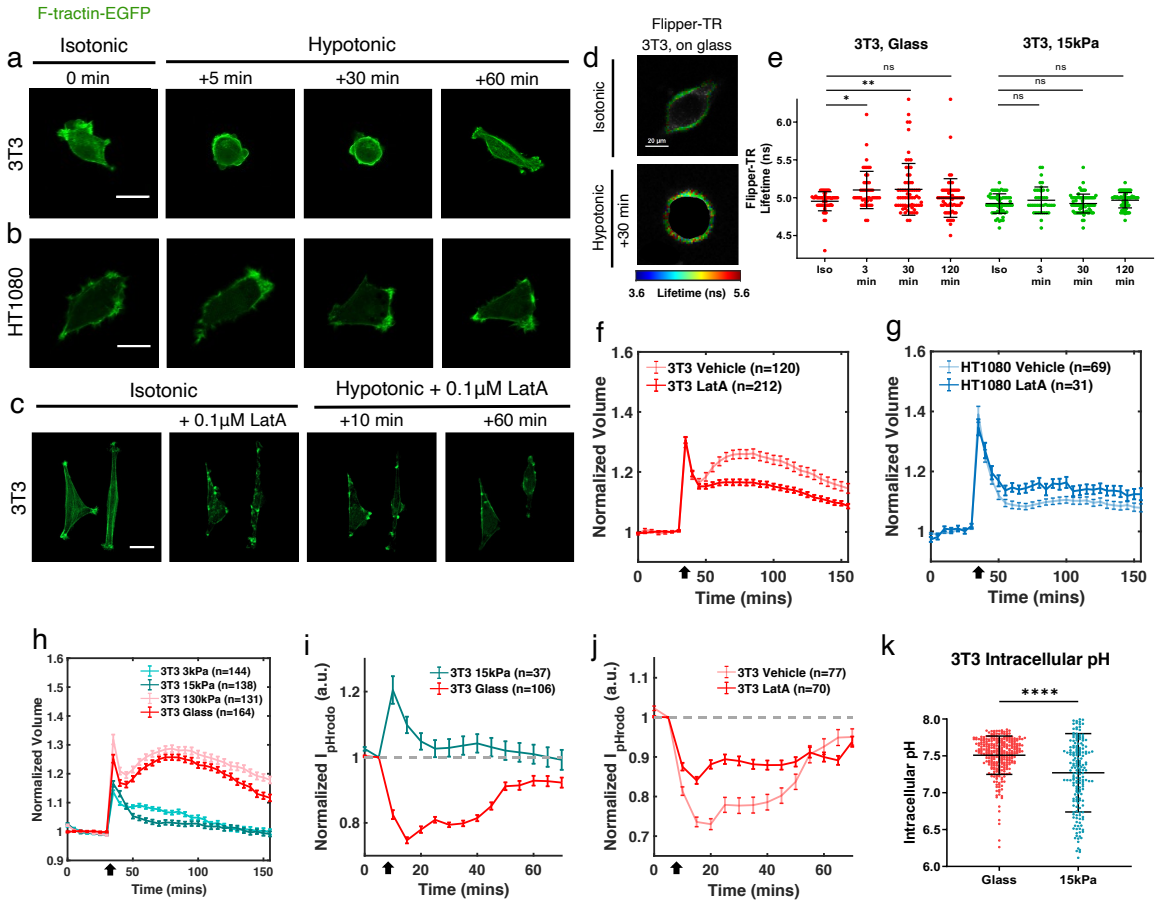

Figure 3: **Actomyosin regulation of cell volume.** (a-c) Confocal images of EGFP-F-tractin transfected 3T3 (a), HT1080 (b), and 3T3 subjected to LatA treatment (c) before and after hypotonic shock. (d) Representative images showing elevated membrane tension measured by Flipper-TR lifetime under hypotonic shock lifetimes in 3T3 on glass. (e) Membrane tension of 3T3 on glass and on 15 kPa PDMS substrate in before and after subjecting to 3 min, 30 min, or 2 h hypotonic shock. n=51, 49, 66, and 60, respectively. (f, g) 3T3 (f) and HT1080 (g) volume dynamics under LatA treatment and hypotonic shock. (h) 3T3 volume dynamics under hypotonic shock on 3, 15, and 130 kPa PDMS substrate and on glass. (i-j) Intensity of pHrodo-red AM for 3T3 on 15 kPa substrate versus on glass (i) and vehicle control versus under LatA treatment (j). Hypotonic shock was applied at 5 mins. (f-j) Error bars indicate SEM. (e, k) Error bars indicate standard deviation. Kruskal–Wallis tests followed by Dunn's multiple-comparison test (e) and Mann–Whitney U test (k). (a-d) Scale bars, 20 μm.

we conclude that SVI generation requires cytoskeletal activity and cell mechanosensation of the mechanical microenvironment.

Our results show that SVI requires an active and intact actomyosin network. However, the lack of SVI under actomyosin disruption appear counterintuitive. Disruption of actomyosin reduces the contractile stress and thus, from the perspective of force balance, should have resulted in a volume increase (*6, 12*). We observed that LatA treatment lowers the cytoplasmic pH after hypotonic shock in 3T3 while having a limited impact on HT1080 (Fig. 3j and Fig. S3f). In addition, 3T3 grown on the compliant substrate also has a lower intracellular pH than those grown on glass, implying lower NHE activity on soft substrate (Fig. 3k). These observations suggest that actomyosin remodeling is required for NHE1 activation during SVI, leading us to postulate that actomyosin regulates the cell volume by mechanically sensing hypotonic stress and signaling to NHE1 rather than directly exerting forces on the cell cortex and membrane.

2.5 Mechanosensitive Ca^{2+} signaling regulates cytoskeletal activation of NHE1

To verify our observation that cell volume is regulated by actomyosin mediated mechanosensation, we examined intracellular Ca^{2+} dynamics, which is known to up-regulate myosin activity through Rho kinase and myosin light chain kinase (*42–44*). Using the Ca^{2+} indicator Gcamp6s, we observed that 3T3 on glass exhibited a greater cytosolic Ca^{2+} increase than HT1080 and 3T3 on soft substrate when subjected to hypotonic shock (Fig. 4a-b). Hypotonic shock also triggered more high-frequency Ca^{2+} spikes in 3T3 on glass than HT1080 and 3T3 on soft substrate (Fig. 4c-d and Fig. S5a-c). Chelating either extracellular Ca^{2+} using BAPTA or intracellular Ca^{2+} using BAPTA-AM (Fig. S5d-e), and blocking mechanosensitive Ca^{2+} channels using $GdCl_3$ or Ruthenium-red (R-red) (Fig. S5f-g) all removed SVI and reduced the steady state cell volume in 3T3. We also validated the similar effect of Ca^{2+} channel blocking in MCF-10A (Fig. S5j). On

the other hand, Ca^{2+} channel blockers had limited impact on HT1080 (Fig. Fig. S5k,l). These results confirm that Ca^{2+} influx via mechanosensitive ion channels is essential in generating the SVI and this mechanism is absent in HT1080 cells.

As one of the highest expressed Ca2+ channel in 3T3 cells (Supplementary Text-1), Piezo1 has been shown to regulate the Ca^{2+} influx triggered by membrane surface expansion (*45–47*). We thus postulated that Piezo1 mediates SVI. Immunostaining of Piezo1 shows that 3T3 on glass forms dense Piezo1 clusters on basal plane (Fig. 4f). HT1080 on glass and 3T3 on soft substrate display a dispersed Piezo1 localization (Fig. 4e,g), which is unfavorable for its focal adhesion dependent activation (*48*). CRISPR knockout of Piezo1 in 3T3 (3T3 Piezo1 KO) abolishes SVI (Fig. 4h) and the intracellular pH decrease when subjected to hypotonic shock (Fig. 4i). To further validate the role of Piezo1 in volume regulation, we activated Piezo1 using its agonist Yoda1 when applying hypotonic shock. Yoda1 triggers faster initial volume recovery (within 3 mins) as well as SVI in both HT1080 and MDA-MB-231 (Fig. S5h,m). Overall, our results indicate that Ca^{2+} influx through the mechanosensitive ion channel Piezo1 is indispensable for SVI during volume regulation triggered by hypotonic stress.

We also asked whether actomyosin directly signals to NHE or through a Ca^{2+}-dependent intermediate. Therefore, we examined ezrin, which crosslinks F-actin with NHE1 at the cell membrane (*49*). The co-localization of actin and NHE1 was confirmed by the immunofluorescence co-staining (Fig. 4j). Next, we examined whether such binding is required for the NHE1 activation during SVI. Blocking ezrin-actin binding via NSC removed SVI (Fig. 4k). Interestingly, NSC treatment had limited effects on the initial recovery of 3T3, and its effect in HT1080 was also insignificant (Fig. S6e). The distinct effect of NSC compared to EIPA treatment is in agreement with our earlier conclusion that SVI is triggered by additional NHE1 activation by actomyosin. This is not required for the initial regulatory volume decrease. This conclusion is further supported by monitoring the intracellular pH in 3T3, where NSC treatment lowered the

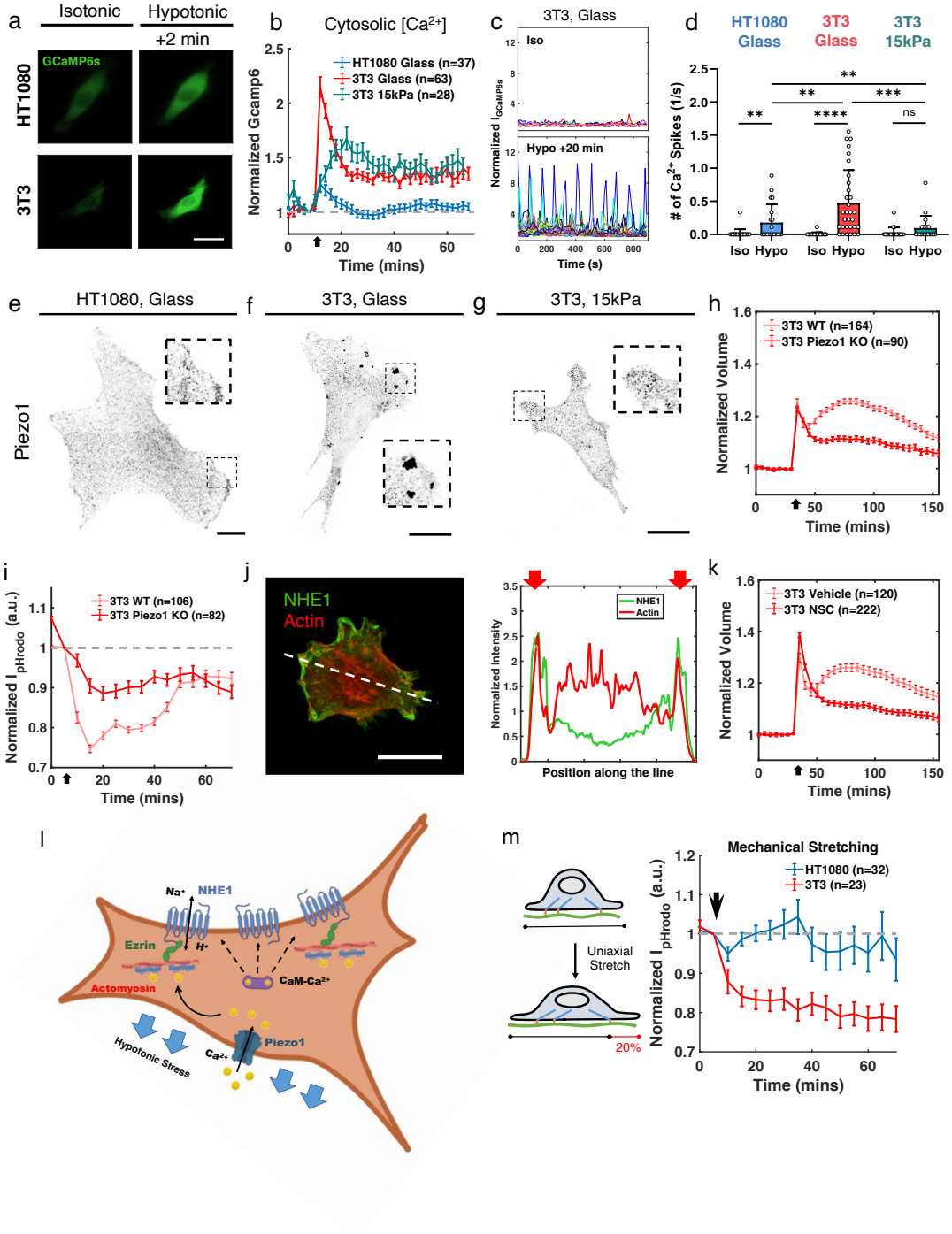

Figure 4: **Mechanosensitive Ca^{2+} dynamics regulates cell volume via actin-NHE1 binding partner ezrin.**

Figure 4: Ca^{2+} influx through Piezo1 regulates cell volume via actin-NHE1 binding partner ezrin. (a) Representative 3T3 and HT1080 GCaMP6s snapshots before and after hypotonic shock. (b) Cytosolic Ca^{2+} concentration of HT1080 on glass, 3T3 on glass, and 3T3 on 15 kPa PDMS substrate measured by GCaMP6s intensity during hypotonic shock (applied at 10 minutes). Imaged at 2-minute frame rate. (c) 3T3 single-cell GCaMP6s dynamics in isotonic media (upper) and 20 minutes after hypotonic shock (lower) on glass. Imaged at 10-second frame rate. (d) The number of Ca^{2+} spikes in isotonic media versus subjected to 20-40 minutes hypotonic shock for HT1080 on glass, 3T3 on glass, and 3T3 on 15 kPa PDMS substrate. The Ca^{2+} spike is defined as at least 2 times GCaMP6 intensity change over the baseline. (e-g) Immunostaining of Piezo1 at the basal plane for HT1080 on glass, 3T3 on glass, and 3T3 on 15 kPa PDMS substrate. (h) 3T3 WT and Piezo1 KO volume dynamics under hypotonic shock (applied at 30 mins). (i) Intensity of pHrodo-red AM for 3T3 WT and Peizo1 KO under hypotonic shock (applied at 5 mins). (j) Co-staining of NHE1 and Actin and their distribution along the line. (k) 3T3 volume dynamics under NSC treatment and hypotonic shock (applied at 30 mins). (l) The proposed signaling pathway that leads to the SVI. (m) pHrodo-red AM intensity of 3T3 and HT1080 under 20% uniaxial mechanical stretch (applied at 5 mins). (e-i, k, m) Error bars indicate SEM. (d) Error bars indicate standard deviation. Mann–Whitney U-tests. HT1080 on glass n = 26 and 20, 3T3 on glass n = 18 and 31, and 3T3 on 15 kPa n = 21 and 20 for isotonic and hypotonic, respectively. (a, e-g, j) Scale bars, 20 µm.

pH during SVI without affecting the pH increase during the initial volume recovery (Fig. S6d). Taken together, our results reveal a mechanosensitive regulatory pathway of cell volume (Fig. 4l): hypotonic stress triggers Ca^{2+} influx through mechanosensitive ion channel Piezo1, inducing actomyosin remodeling that further activates NHE1 through their synergistic binding partner ezrin, leading to SVI.

Similar to hypotonic shock, expanding cell surface by mechanical stretch has been reported to trigger Ca^{2+} influx through Piezo1 (*45*), and we postulated it can also activate NHE1 through the same mechanosensitive pathway. Indeed, applying a one-time, 20% uniaxial stretch to 3T3 led to an immediate pH increase (Fig. 4m). On the contrary, mechanical stretch did not alter the pH in HT1080. Consistent with the hypotonic shock experiment, knocking out Piezo1 or treating 3T3 with NSC or LatA abolished or reduced the immediate pH change under mechanical stretch (Fig. S6f-h). These results support the idea that NHE1 can be mechanically activated by Ca^{2+} and the actin cytoskeleton.

Calmodulin (CaM) is an ubiquitous Ca^{2+} receptor that has been shown to bind to NHE1 (*28, 29, 50*). To examine whether Ca^{2+}-CaM regulates NHE1 activity, we treated cells with a

Ca^{2+}-CaM antagonist, W7. Addition of W7 halts F-actin remodeling under hypotonic shock (Fig. S6a), and remarkably accelerated the initial regulatory volume decrease in all four cell lines tested as well as removing SVI in 3T3 and MCF-10A (Fig. S6b,c, i, j), similar to EIPA treatment (Fig. 2e,f, and Fig. S2c,d). Addition of W7 also significantly lowers the pH in 3T3 following hypotonic shock (Fig. S6k), indicating that Ca^{2+}-CaM is also required for NHE1 activation.

2.6 Cytoskeletal activation of NHE1 deforms nucleus , demethylates DNA, and modifies transcriptomic profile

Recent studies have revealed the important role of the nucleus in sensing mechanical forces (*51–54*). To examine whether the cell nucleus responds to hypotonic stress, we stained cells with Hoechst 33342 and monitored nucleus size change under hypotonic shock. HT1080 exhibited an immediate $\sim$ 10% increase in nuclear area (Fig. 5a-b), consistent with previous reports (*55*). In contrast, 3T3 cells initially exhibited a $\sim$ 20% reduction in nuclear area, followed by a gradual increase until reaching a similar $\sim$ 10% increase as HT1080. During nucleus deformation, the fraction of regions with high Hoechst intensity (heterochromatin) also increased in 3T3 but not in HT1080 (Fig. S7d), suggesting that 3T3 re-organized chromatin under hypotonic stress. We noticed that the onset and the timescale of nucleus area recovery coincided with SVI in 3T3, and thus we hypothesized that nucleus deformation is associated with Ca^{2+}-cytoskeleton mediated NHE1 activation. Indeed, EIPA treatment hindered the nucleus area recovery in 3T3 (Fig. 5c), while treating 3T3 with LatA or NSC, or knocking out Piezo1 abolished the nucleus area change under hypotonic shock (Fig. S7a-c). These drugs or Piezo1 KO also impeded chromatin re-organization (Fig. S7e-h).

To determine whether hypotonic stress induced nucleus deformation and chromatin re-organization resulted in cell epigenetic modification, we quantified DNA methylation levels by

staining 5-Methycytosine (5-mC). We found that exposing 3T3 to a hypotonic environment for 1 h reduced 5-mC level by 51%(Fig. 5d-e), similar to the levels seen during mechanical confinement and nucleus compression (*56*). The 5-mC reduction peaked 2h after shock, then gradually recovered, culminating in an increase after 24 hours (Fig. S7i). On the other hand, HT1080 exhibited only a 16% reduction in 5-mC levels (Fig. S7j). Disrupting Ca^{2+}-cytoskeleton mediated NHE1 activation using EIPA, LatA, NSC, or knocking out Piezo1 abolished the DNA de-methylation in 3T3, resulting in 5-mC expression reductions of 9%, 14%, 7%, and 1%, respectively, compared with 57% reduction for vehicle control. Similarly, soft substrates attenuated the hypotonic shock induced DNA de-methylation (Fig. S7k). These results suggest that the cytoskeletal activation of NHE1 is vital in regulating chromatin modification post hypotonic shock. Both this chromatin regulatory mechanism and SVI are absent in HT1080 cells.

The substantial DNA de-methylation observed under hypotonic conditions motivated us to further examine the transcriptomic profiles using RNA sequencing (RNA-Seq). Principal component analysis (PCA) clustered all conditions into 3 transcriptomic states: isotonic, 2-hour hypotonic shock, and 24-hour hypotonic shock, for both 3T3 and HT1080 cell lines regardless of LatA treatment (Fig. 5f and Fig. S8a). Differentially expressed genes (DEGs, defined as adjusted $p<0.05$) at 2-hour hypotonic shock versus isotonic condition suggest that 3T3 cells initiated a much pronounced, short-timescale transcriptomic response to hypotonic shock that is not observed in HT1080 cells (2531 DEGs for 3T3 versus 192 DEGs for HT080, Fig. 5g,h), in line with their distinct DNA demethylation levels. Ingenuity Pathway Analysis (IPA, Ref. 57) identified the tumor necrosis factor (TNF) signaling pathway as the primary upstream pathway responding to hypotonic shock in both 3T3 and HT1080, but the downstream pathways are distinct in each cell line (Fig. S8g,h). The number of DEGs increased at 24 hours after hypotonic shock for both cell lines (Fig. S8b,c), indicating hypotonic shock triggers a long-lasting transcriptomic response.

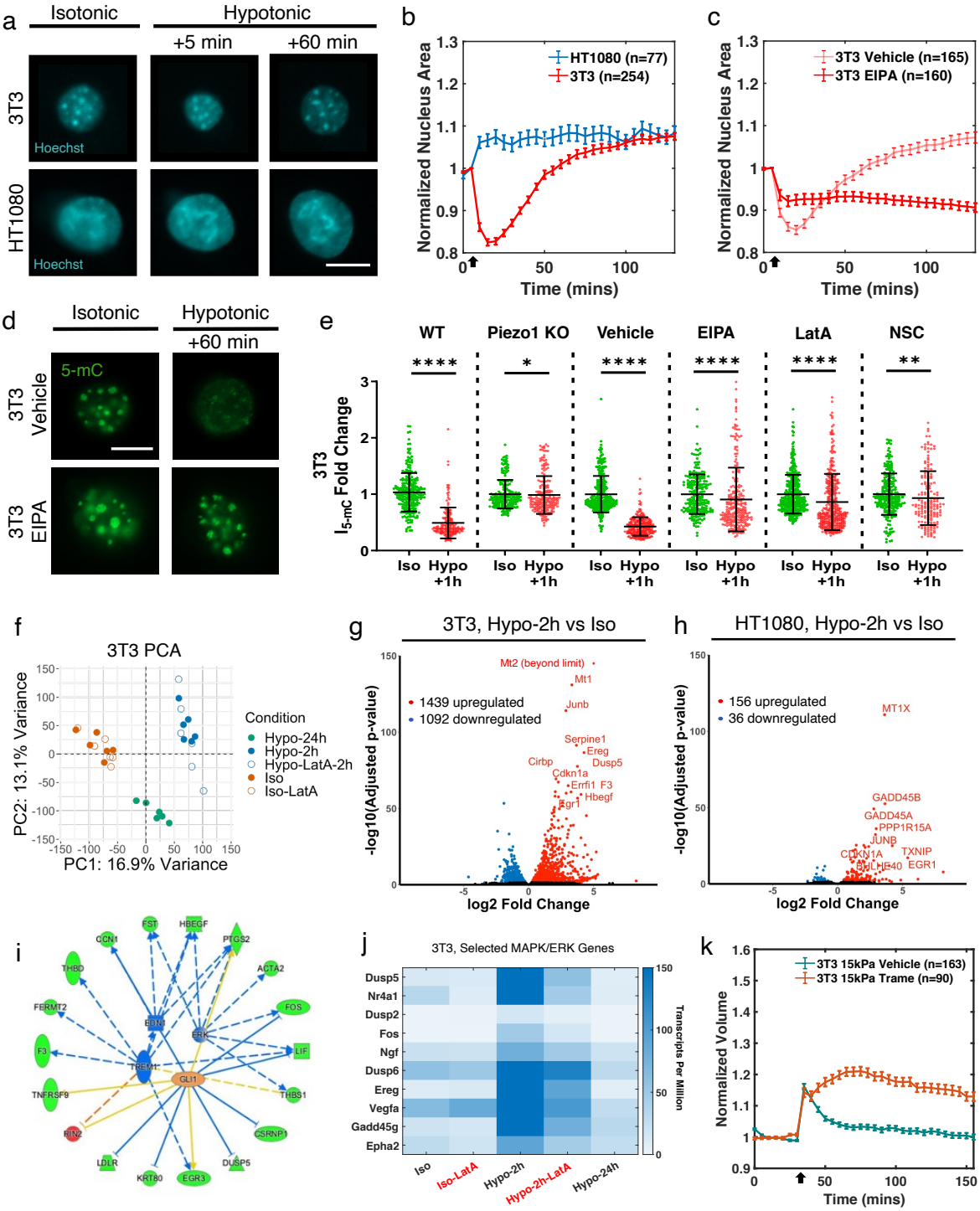

Figure 5: **Hypotonic shock induces nucleus deformation and DNA de-methylation.**

Figure 5: Hypotonic shock induces nucleus deformation and DNA de-methylation. (a) Representative nuclei images of 3T3 and HT1080 stained with Hoechst 33342 from live single cell tracking. (b) Normalized nucleus area of 3T3 and HT1080 with hypotonic shock applied at 5 min. (c) Normalized nucleus area of 3T3 treated with 100 μM EIPA and vehicle control. Hypotonic shock was applied at 5 min. (d) Representative immunofluorescence images of 3T3 staining 5-Methycytosine (5-mC) treated with EIPA and vehicle control. Cells were fixed in isotonic condition or after exposing to hypotonic environment for 1 h. (e) Fold change of 3T3 5-mC expression level in isotonic condition *versus* 1 h exposure to hypotonic condition from immunofluorescence. (f) Principle component analysis (PCA) for 3T3 before and after hypotonic shock and with or without LatA treatment. N = 3 biological repeats. (g, h) Volcano plots showing DEGs at 2-hour hypotonic shock versus in isotonic media for 3T3 (g) and HT1080 (h). (i) Top 4 upstream pathway identified by Ingenuity Pathway Analysis in 3T3 2-hour hypotonic shock with and without LatA treatment. Red/green indicates increased/decreased measurement, and orange/blue indicates predicated activation/deactivation. (j) Gene heatmap showing expression of MAPK/ERK pathway genes identify in (i). (k) Volume dynamics of 3T3 on glass versus 15 kPa with Trametinib (Trame, MEK/ERK inhibitor) treatment and hypotonic shock (applied at 30 minutes). (b, c, k) Error bars indicate SEM. (e) Error bars indicate standard deviation. Mann–Whitney U test. n = 161-366 per condition. (a, d) Scale bars, 10 μm.

We next examined how disrupting SVI using LatA impacted transcriptomics. We identified 171 DEGs in 3T3 under 2-hour hypotonic shock with LatA treatment comparing to untreated condition (Fig. S8d). IPA highlights several MAPK/ERK genes as most significantly inhibited by disrupting SVI (Fig. 5i). Interestingly, LatA treatment suppresses the up-regulation of Dusp5 and Dusp6 observed under 2h hypotonic shock (Fig. 5j). These genes encode phosphatases that inactivates ERK1/2, suggesting ERK inhibition is associated with SVI. To further probe this, we treated 3T3 grown on compliant substrate with the MEK/ERK inhibitor Trametinib (Trame). ERK inhibition restored SVI and triggered pH increase upon hypotonic shock, supporting our hypothesis (Fig. 5k and Fig. S8f). On the other hand, HT1080 transcriptomics are less sensitive to LatA and no ERK dependence is observed (Fig. S8e). Taken together, these findings reveal the impact of hypotonic shock in modulating transcriptomic responses and emphasize the pivotal role of the actomyosin and MAPK/ERK pathway in SVI.

3 Discussion

Recent studies have revealed the importance of physical variables such as adhesions and forces in cell size regulation. However, except for a WNK-activated Cl^- secretion mechanism during hypertonic volume decrease (*58*), a detailed mechanism of how cells regulate volume during hypotonic expansion has yet to be revealed. In this paper, we showed that the initial phase of rapid regulatory volume decrease under hypotonic stress can be explained by rapid actions of ion channels/pumps. However, cells can further regulate their volume by mechanically activating NHE1 through a signaling cascade involving Ca^{2+}, actomyosin and ezrin. In 3T3, hypotonic stress triggers Ca^{2+} influx through Piezo1 that further activates myosin activity. The remodeling of actomyosin network signals to NHE1 through their synergistic linker Ezrin, triggering SVI after the initial volume recovery. A similar mechanical activation of NHE1 can also be achieved by expanding cell surface using uniaxial stretching. Remarkably, soft substrate abolishes SVI generation. We further show that the hypotonic shock induced mechanosensory response can deform the cell nucleus, and the subsequent NHE activity is linked to significant DNA de-methylation and transcriptomic change. This mechanosensory mechanism of cell volume regulation is largely absent in HT1080 and some other types of cancer cells. The differential mechanisms of volume regulation may be a defining feature of transformed and malignant cells.

Despite their low concentrations in cytoplasm, our findings highlight the critical role of Ca^{2+} and pH in regulating cell volume through both direct binding and activation of NHE1 via Calmodulin and induction of actomyosin remodel that indirectly activates NHE1 via ezrin. Interestingly, disrupting the actin network or blocking actin-ezrin binding had limited impact on the initial regulatory volume decrease (Fig. 3f,g, and j, Fig. 4k, Fig. S6e), suggesting that the cytoskeletal activation of NHE1 observed during SVI and mechanical stretch is a regula-

tory response to environmental change, rather than a continuous process during stationary cell culture.

The magnitude and the timescale of the observed SVI and the corresponding shape change (rounding up) in 3T3 is intriguingly similar to mitotic cell swelling, a phenomenon that has been shown to be regulated by actomyosin and NHE (*5, 6, 59*). This correspondence suggests that cells potentially regulates their mitotic entry through Ca^{2+} mediated mechanosensation to ion channels/transporters. Chromosome modification associated with NHE mediated swelling maybe important for successful mitosis. This hypothesis should be examined in future work, although we note that in HT1080 cells that lacks SVI, mitotic swelling is still present. In addition, a series of recent works showed that water flux driven by ion transport is responsible for cell migration in 1D confinement and 2D environments, and NHE is one of the central players activated by actomyosin dynamics (*8, 10, 11, 17*). These results hint that the cell volume dynamics is associated with cell migration, and the mechanical activation of NHE1 is another way for cells to generate protrusions and motility. Actin and myosin serve as sensory and control elements during this type of protrusion, but forces are generated by NHE and water influx to propel the cell. Moreover, the distinct responses to mechanical cues and pharmacological treatments suggest that there are potentially multiple pathways. For example, recent works suggest a potential crosstalk between microtubules and the mTorc pathway that regulates cell volume response mediated by osmotic pressure and curvature of the substrates (*15, 21*). A comprehensive understanding of short timescale cell volume regulation requires a tool that can accurately measure intracellular osmolarity, which is still lacking. We identified the importance of stretch-activated channel Piezo1 in cell volume regulation, but the roles of other mechanosensitive Ca^{2+} channels or store-operated channels need to be explored in the future.

Materials and Methods

Cell Culture, osmotic shock media preparation, and pharmacological inhibitors

NIH 3T3 and HT1080 were a gift from D. Wirtz (Johns Hopkins University, Baltimore, MD). MCF-10A and MDA-MB-231 were purchased from American Type Culture Collection. 3T3, HT1080, and MDA-MB-231 were cultured in Dulbecco's modified Eagle's media (Corning) supplemented with 10% fetal bovine serum (FBS; Sigma), and 1% antibiotics solution contains 10,000 units/mL penicillin and 10,000 µg/mL streptomycin (Gibco). MCF-10A were cultured in DMEM/F-12 supplemented with 5% horse serum, 20 ng/mL Epidermal Growth Factor, 0.5 µg/mL hydrocortisone, 100 ng/mL cholera toxin, 10 µg/mL insulin, and 1% antibiotics solution, as previously described (*60*). Cells were passaged using 0.05% trypsin-EDTA (Gibco). All cell cultures and live cell experiments were conducted at 37 °C and 5% CO2.

Before hypotonic shock experiment, cells were pre-incubated in isotonic solution overnight. The isotonic solution (312 mOsm) contains 50% Dulbecco's phosphate-buffered saline without calcium and magnesium (Sigma-Aldrich) and 50% cell culture media. 50% hypotonic media (175 mOsm) was prepared by mixing 50% ultra-pure water with 50% cell culture media. For hypertonic shock experiment, cells were cultured in regular cell culture media, and then switched to 50% hypertonic media (504 mOsm). The hypertonic media is the cell culture media supplemented with 160 mM D-Sorbitol (MilliporeSigma). The osmolality was measured using Advanced Instruments model 3320 osmometer.

In select experiments, cells were treated with the following pharmacological agents (purchased from Tocris unless otherwise stated): vehicle controls using DMSO (0.25%, Invitrogen), Latrunculin A (100 nM), Cytochalasin D (500 nM), (S)-nitro-Blebbistatin (1 µM, Cayman Chemical), W7 hydrochloride (20 µM), NSC668394 (10 µM, MilliporeSigma), Ouabain (250 µM), EIPA (100 µM for 3T3, 50 µM for other cell lines), Bumetanide (40 µM), DCPIB (20

μM, Medchemexpress), 4-Aminopyridine (4-AP, 1 mM), Ruthenium red (20 μM), Gadolinium chloride (GdCl3, 20 μM), BAPTA Tetrapotassium Salt (1mM, Invitrogen), BAPTA-AM (5 μM, Invitrogen), and Trametinib (0.2 μM, Medchemexpress). In osmotic shock experiment, cells were pre-adapted in pharmacological agents for 2h expect for Latrunculin A (1 h), Cytochalasin D (1 h), EIPA (1 h), and Ouabain (4 h).

Microfluidic device fabrication

A detailed protocol can be found in Ref. 32. In brief, FXm channel masks were designed using AutoCAD and ordered from FineLineImaging. Silicon molds were fabricated using SU8-3010 (Kayaku) photoresist following standard photolithography procedures and manufacturer's protocol. Two layers of photoresist were spin coated on a silicon wafer (IWS) at 500 rpm for 7 s with acceleration of 100 rpm/s, and at 2,000 rpm for 30 s with acceleration of 300 rpm/s, respectively. After a soft bake of 4 min at 95 °C, UV light was used to etch the desired patterns from negative photoresist to yield feature heights that were $\sim$12 μm. The length of the channels is 16 mm and the width is 1.2 mm.

A 10:1 ratio of PDMS Sylgard 184 silicone elastomer and curing agent were vigorously stirred, vacuum degassed, poured onto each silicon wafer, and cured in an oven at 80 °C for 45 min. Razor blades were then used to cut the devices into the proper dimensions, and inlet and outlet ports were punched using a blunt-tipped 21-gauge needle (McMaster Carr; 76165A679). The devices were cleaned by sonicating in 100% isopropyl alcohol for 10 min, and dried using a compressed air gun. The devices and sterilized 50-mm glass-bottom Petri dishes (FlouroDish Cell Culture Dish; World Precision Instruments) were exposed to oxygen plasma for 1 min for bonding. The bonded devices were then placed in an oven at 80 °C for 45 min to further ensure bonding.

Cell volume tracking under pharmacological inhibition and osmotic shock experiment

Micro-fluidic FXm chambers were incubated with 50 µg/mL of type I rat-tail collagen (Enzo) for 1 h at 37 °C, followed by washing with isotonic media. Before experiment, $\sim$ 1-2 million per mL cells with 0.2 mg/mL Alexa Fluor 488 Dextran (MW 2,000 kDa; ThermoFisher) dissolved in isotonic media were injected into the devices using syringe. Cells were then incubated for 1-2 h to allow them to attach and spread. To apply drug or osmotic shock, hypotonic or hypertonic media were injected into the channel gently using a syringe with the same amount of dextran. For osmotic shock experiment with drug treatment, cells were pre-adapted 1-4 h in the FXm device before applying osmotic shock. For cell nucleus area tracking, cells were stained with Hoechst 33342 (1:10000) for 10 min at 37 °C in suspension before seeding into the FXm channel. Cells were imaged using fluorescence microscopes as detailed below. The microscope was also equipped with a CO2 module and TempModule stage top incubator (Pecon) that was set to 37 °C and 5% CO2 during the experiment. Biological repeat with sample size N $\geq$ 3 for all experiments.

Data analysis and cell volume calculation in Fluorescence Exclusion method

Individual cells were tracked by customized MATLAB code using the following algorithm. Firstly, a rough cell mask was draw from a Gaussian blurred epifluorescence image by a set threshold intensity for each cell. The cell mask was then expanded by 100 pixels (2.27 µm) in each direction to ensure proper cell cropping, and a rectangular box was draw based on the largest lateral dimensions in x and y direction. A cell would be discarded if any overlapping cells were found in the box. After all images at different time points were processed, we ran an automatic cell tracking algorithm based on the position of geometric center of each cell mask. In brief, the algorithm assigned each cell (C_t) to the closest cell in the next time frame ($C_{t+\Delta t}$), and

then cross validated the tracking by assigning $C_{t+\Delta t}$ to its closest cell at frame t. The cell would be discarded if the cross validation failed to find C_t as the closest neighbor or found more than one closest neighbor, which is normally due to cell migration, detachment, or overlapping with other cells. The results from automatic cell tracking algorithm were then examined manually by one of the authors.

Cropped images from single cell tracking were then used for cell volume calculation based on the Fluorescence Exclusion method (FXm). The mean fluorescence intensity of the pixels outside cell masks, defined as the mean background intensity I_{bg}, reflects the height of the FXm channel. The local intensity within the cell mask, I_V defined the difference between channel height and cell height. Given a known channel height h, measured by confocal microscopy, the cell volume V can be calculated using the equation $V = h \iint_A (1 - \frac{I_V}{I_{bg}})\, dA$.

Epi-fluorescence and confocal microscopy

For epi-fluorescence imaging, a Zeiss Axio Observer inverted, wide-field microscope using a 20× air, 0.8-NA objective or a 63× oil-immersion, 1.2-NA objective equipped with an Axiocam 560 mono charged-coupled device camera was used. In some experiments, a similar microscope equipped with a Hamamatsu Flash4.0 V3 sCMOS camera was used. For confocal imaging, a Zeiss LSM 800 confocal microscope equipped with a 63× oil-immersion, 1.2-NA objective was used. All microscopes were equipped with a CO2 Module S (Zeiss) and TempModule S (Zeiss) stage-top incubator (Pecon) that was set to 37 °C with 5% CO2 for live cell imaging. For imaging of immunofluorescence assays, the samples were imaged under room temperature and without CO2. ZEN 2.6 or 3.6 Software (Zeiss) was used as the acquisition software. Customized Matlab (MathWorks) programs or ImageJ were used for image analysis subsequent to data acquisition.

Measurement of membrane tension using Fluorescence Lifetime Imaging microscopy

Cells were seeded into collagen-I coated (50 µg/mL for 1 h at 37 °C) glass bottom 24 well plates or 35 mm glass bottom dish coated with 15 kPa PDMS substrate at a density of 5000 cells/cm^2 in isotonic media overnight. Cells were stained with 1 µM Flipper-TR (Spirochrome) for 30 min and imaged thereafter. Hypotonic shock was then conducted, and cells were imaged 3 min, 30 min, and 2 h after shock. Confocal fluorescence lifetime imaging microscopy was performed using a Zeiss LSM 780 microscope and a PicoQuant system consisting of a PicoHarp 300 time-correlated single-photon counting (TCSPC) module, two-hybrid PMA-04 detectors, and a Sepia II laser control module. A 485 nm laser line was used for excitation with a 600/50 nm band-pass detector unit. Cells were maintained at 37 °C with 5% CO2 in a Pecon incubator during imaging. The data analysis was performed as previously described (*61*) using SymPhoTime 64 (PicoQuant) software.

PDMS substrate fabrication

3 kPa PDMS substrate was prepared by mixing a 1:1 weight ratio of CY52-276A and CY52-276B (Dow) (*18*). To generate 15 kPa and 130 kPa substrates, 2% and 20% Sylgard 527 (Dow, 1:1 base to curing agent ratio) were added to Sylgard 184 (Dow, 10:1 base to curing agent ratio), respectively (*62*). In all cases, the elastomer was vacuum-degassed for approximately 5 min to eliminate bubbles, and then spin-coated onto 35 mm or 50 mm glass bottom dishes at 1,000 rpm for 60 s. The dishes were cured overnight at room temperature, and then at 80 °C for 20 min. The devices were subsequently plasma-treated and bonded to the FXm devices for cell volume measurement.

Cloning, lentivirus preparation, transduction, and transfection

To generate 3T3 cells with stable knockdown of NHE1, the pLKO.1 puro (Addgene; 8453; a gift from Bob Weinberg) backbone was used. For NHE1 depletion, the sequence 5'-GACAAGCTCAACCGGTTTAAT-3' was subcloned into the pLKO.1 backbone. For generating control cell lines, the non-targeting scramble control sequence 5'-GCACTACCAGAGCTAACTCAGATAGTACT-3' was subcloned into the pLKO.1 puro backbone.

For lentivirus production, HEK 293T/17 cells were co-transfected with psPAX2, VSVG, and the lentiviral plasmid of interest. 48 h after transfection, the lentivirus was harvested and concentrated using centrifugation. Wild-type 3T3 cells at 60-80% confluency were incubated for 24 h with 100X virus suspension and 8 µg/ml of Polybrene Transfection Reagent (Millipore Sigma). To maintain stable knockdown, cells transduced with the pLKO.1 puro backbone or sgBag6_1 with Ef1alpha Puro-P2A-BFP(1)(1) backbone were cultured in medium containing 0.5 µg/ml Puromycin (Gibco).

Live cell reporters

pEGFP-C1 F-tractin-EGFP (Addgene 58473, a gift from Dyche Mullins) plasmids were used for transient transfections. About 60-80% confluent 3T3 or HT1080 cells were transfected using Lipofectamine 3000 reagent following the manufacturer's recommendations. pHAGE-RSV-GCaMP6s (Addgene 80146, a gift from Darrell Kotton) plasmids were used for lentiviral cell transduction. The lentivirus production is described above, and cells were selected using flowcytometry.

CRISPR knockout

Single guide RNA (sgRNA) against PIEZO1 that targets the 5'-AGCATTGAAGCGTAACAGGG-PAM-3' at Chr.8: 122513787 - 122513809 on GRCm38 was purchased from Invitrogen (A35533). The cells were transfected with the Cas9 enzyme (TrueCut Cas9 Protein v2, Thermo Fisher) and the sgRNA using Lipofectamine™ CRISPRMAX™ Transfection Reagent (Thermo Fisher) according to the manufacturer's instructions. Transfected cells were then expanded as single-cell clones by limited dilution into 96 well plates. To evaluate the editing efficiency, GeneArt Genomic Cleavage Detection Kit (Life Technologies) was used according to the manufacturer's instructions. Then, the following primers were used to amplify the region covering the CRISPR binding site: TATCATGGGACCTGGGCATC (forward), CAGGTGTGCACTGAAG-GAAC (reverse). The knockout of Piezo1 was confirmed by next generation sequencing (NGS, provided by Genewiz) and western blot (Fig. S5i).

Immunofluorescence and image analysis

Cells were seeded into collagen-I coated (50 µg/mL for 1 h in 37 °C) glass bottom 24 well plates or 35 mm glass bottom dish coated with 15kPa PDMS substrate at a density of 5000 cells/cm^2 overnight. For pMLC staining, hypotonic shock was applied and cells were fixed with 4% paraformaldehyde (ThermoFisher Scientific) at different time points as indicated. After washing 3X with PBS, cells were permeabilized in 0.1% Triton X-100 for 15 minutes. Then, cells were washed 3X in PBS and blocked for 1 h at RT with 5% BSA solution containing 5% normal goat serum (Cell Signaling) and 0.1% Triton X-100. Next, cells were incubated at 4°C with primary antibody overnight. After washing 3X with PBS, samples were incubated for 1 h at RT with secondary antibody. NHE1 staining follows the same protocol as described above but without osmotic shock. For 5-methyCytosine staining, cells were fixed with ice-cold 70% ethanol for 5 mins. After 3X washes in PBS, samples were treated with 1.5 M HCl for 30

minutes, followed by 3 washes in PBS. Then, the staining follows the same protocol proceeded from blocking as mentioned above. Primary antibody: anti-pMLC (Ser19) antibody (Cell Signaling; 3671; 1:100), anti-NHE1 (Invitrogen; PA5-116471; 1:100), anti-Piezo1 (Invitrogen; PA5-77617; 1:500), and anti-5-Methycytosine (Cell Signaling; 28692S; 1:500). Secondary antibody: Alexa Fluor 488 goat anti-rabbit immunoglobulin G (IgG) H+L, (Invitrogen; A11008; 1:200). For actin staining, Alexa Fluor 647 Phalloidin (Invitrogen; A22287; 1:100) were added for 1h at RT. For nucleus staining, Hoechst 33342 (Invitrogen; H3570; 1:10000) were added for 10 minutes at RT.

Wide-field microscopy using the setup as described above was used to measure the total pMLC and 5-mC contents. A rectangle was cropped for each cell, and the boundary of the cropped area was used for calculating background intensity. The total expressed protein contents of each cell were quantified by summing all intensity after background subtraction. To evaluate 5-mC expression, cell nucleus masks were drawn based on the Hoechst channel after cropping and background subtraction as aforementioned. The nucleus mask was then applied to 5-mC staining images to measure the total intensity within each cell nucleus. The spatial distribution of NHE1 and actin was obtained using a confocal microscope as described above. A line was drawn along the cell to obtain the spatial distribution of NHE1 and actin using ImageJ.

Western Blot

Western blots were performed using protocols previously described in Ref.51, using NuPAGE™ 4-12% Bis-Tris Protein Gels (Thermo Fischer Scientific, NP0336BOX) in Invitrogen Novex NuPage MES SDS Running Buffer (1X, Thermo Fisher Scientific, NP0002). Primary antibody: anti-NHE1 (Santa Cruz Biotechnology; sc-136239; 1:1000), and anti-Piezo1 (Invitrogen; PA5-77617; 1:1000). GAPDH was used as a loading control (Cell Signaling; 2118S; 1:4000). Secondary Antibody: anti-mouse IgG, HRP-linked antibody (Cell Signaling; 7076S; 1:1000), and

anti-rabbit IgG HRP-linked antibody (Cell Signaling, 7074S; 1:1000).

Intracellular pH measurement

Intracellular pH was measured using pHrodo Red AM, following the manufacturer's instructions. Cells were seeded into collagen-I coated (50 µg/mL for 1 h at 37 °C) glass bottom 24 well plates or 35 mm glass bottom dish coated with a 15kPa PDMS substrate at a density of 5000 cells/cm^2 overnight in isotonic media. Cells were then incubated with 1ml of media containing a dilution of 1 µL of 5 mM pHrodo Red AM in 10 µL of PowerLoad 100X concentrate at 37°C for 45 minutes. The cells were gently washed once with media and allowed to settle for 15 minutes before imaging. Cells before and after hypotonic shock were imaged every 5 minutes using a wide-field epi-fluorescence microscope as previously described. A rectangle larger than the cell size was cropped for each cell, and the signal at the boundary of each cropped area was used to calculate background intensity. pHrodo Red AM signals of individual cells were tracked and measured as the total intensity within the cropped area after background subtraction.

To obtain the absolute pH of different cell types, an intracellular pH calibration buffer Kit (Invitrogen, P35379) was used with pHrodo Red AM, following the manufacturer's protocol. Briefly, after loading pHrodo Red AM as instructed above, cells were then loaded with the calibration buffer containing 10 µM valinomycin and 10 µM of nigericin at pH values of 4.5, 5.5, 6.7, and 7.5 for at least 5 minutes. The cells were then imaged and processed through the same background subtraction as described above. Cells were masked, and the mean intensity per pixel was calculated for each cell. A pH calibration curve was then generated by linearly fitting the results from the calibration experiment. Single cell pHrodo intensity was measured, processed, and fitted into the calibration curve to obtain single cell pH results.

Mechanical stretching

Cells were seeded into elastic PDMS chambers (STB-CH-4W, STREX) at a density of 5000 cells/cm^2 with cell culture media. The PDMS chambers were pre-coated with 200 µg/mL collagen-I (Enzo) for 4 h at 37 °C. A one-time, 20% uniaxial stretching was applied using a mechanical stretching device (STB-100, STREX). pH measurement and data analysis were conducted as described above. Mechanical stretching may cause cell detachment; therefore, only cells that remained attached and spread both before and after mechanical stretching were analyzed.

Calcium dynamics imaging and quantification

Cells transiently expressing pGP-CMV-GCaMP6s were seeded into collagen I coated, glass bottom 24 well plate overnight at a density of 5000 cells/cm^2. For low frequency Ca^{2+} dynamics, cells before and after hypotonic shock were imaged every 2 minutes using the confocal microscope as described above. Ca^{2+} dynamics were monitored by the mean cell GFP signals per pixel using the image processing method as described above. To measure Ca^{2+} spikes, cells in isotonic media or subjected to hypotonic shock for 20 minutes were imaged every 10 seconds using the confocal microscope. Ca^{2+} spikes were identified as instances with greater than 2 times intensity over baseline signals.

RNA-seq and analysis

Total RNA was extracted and purified using RNeasy Mini Kit (Qiagen) following the manufacturer's protocol. Strand specific mRNA libraries were generated using the NEBNext Ultra II Directional RNA library prep Kit for Illumina (New England BioLabs #E7760), mRNA was isolated using Poly(A) mRNA magnetic isolation module (New England BioLabs #E7490). Preparation of libraries followed the manufacturer's protocol (Version 2.2 05/19). Input was

1ug and samples were fragmented for 15 min for RNA insert size of 200 bp. The following PCR cycling conditions were used: 98°C 30s / 8 cycles: 98°C 10s, 65°C 75s / 65°C 5 min. Stranded mRNA libraries were sequenced on an Illumina NovaSeq instrument, SP flowcell using 100bp paired-end dual indexed reads and 1% PhiX control.

Reads were trimmed by 8 base pairs on either end with the Cutadapt package and mapped to the mouse GRCm38 (mm10) or human GRCh38 (hg38) using the Salmon package. Reference genomes were obtained from Ensemble. Batch correction was performed in R with ComBat seq. In R (v.4.2.3), the DESeq2 package was used to determine differentially expressed genes between samples of interest with P values for each gene and comparison. P values were calculated with the DESeq2 package, assuming a negative binomial distribution and correcting for FDR. Differentially expressed genes with an FDR corrected P value $<= 0.05$ were presented in volcano plots and further analyzed. The significantly differentially expressed genes with a log2 fold change $<=$ -1 or $>=$ 1 were input into Ingenuity Pathway Analysis (Qiagen) to determine pathway enrichment (significance determined by Fischer's exact method).

Statistical analysis

For time series plots, error bars represent the mean and the standard error of mean of at least 3 biological repeats. The number of cells analyzed per condition were noted in the plots or in the captions. For scatter plots, error bar represent the mean and the standard deviation of at least 3 biological repeats. D'Agostino–Pearson omnibus normality test was used to determine whether data were normally distributed. For non-Gaussian distributions, nonparametric Mann–Whitney U-tests were used comparing two conditions, and comparisons for more than two groups were performed using Kruskal–Wallis tests followed by Dunn's multiple-comparison test. The statistical analysis was conducted using MATLAB 2021b(Mathworks), or GraphPad Prism 9 or 10 (GraphPad Software). Statistical significance was identified as $p<0.05$. *$p<0.05$, **$p<0.01$,

***p<0.001 and ****p<0.0001.

References

1. E. K. Hoffmann, I. H. Lambert, S. F. Pedersen, *Physiological Reviews* **89**, 193 (2009).

2. M. B. Ginzberg, R. Kafri, M. Kirschner, *Science* **348** (2015).

3. C. Cadart, *et al.*, *Nature Communications* **9** (2018).

4. E. Zlotek-Zlotkiewicz, S. Monnier, G. Cappello, M. Le Berre, M. Piel, *Journal of Cell Biology* **211**, 765 (2015).

5. S. Son, *et al.*, *Journal of Cell Biology* **211**, 757 (2015).

6. M. P. Stewart, *et al.*, *Nature* **469**, 226 (2011).

7. O. M. Lancaster, *et al.*, *Developmental cell* **25**, 270 (2013).

8. K. M. Stroka, *et al.*, *Cell* **157**, 611 (2014).

9. J. Tao, Y. Li, D. K. Vig, S. X. Sun, *Reports on Progress in Physics* **80** (2017).

10. Y. Li, K. Konstantopoulos, R. Zhao, Y. Mori, S. X. Sun, *Journal of cell science* **133** (2020).

11. K. Bera, *et al.*, *Nature* **611** (2022).

12. H. Jiang, S. X. Sun, *Biophysical Journal* **105**, 609 (2013).

13. C. Cadart, L. Venkova, P. Recho, M. C. Lagomarsino, M. Piel, *Nature Physics* **15**, 993 (2019).

14. J. Tao, S. X. Sun, *Biophysical Journal* **109**, 1541 (2015).

15. C. Roffay, *et al.*, *Proceedings of the National Academy of Sciences of the United States of America* **118** (2021).

16. L. Venkova, *et al.*, *eLife* **11** (2022).

17. D. Maity, *et al.*, *Advanced Science* **9**, 2200927 (2022).

18. N. P. Gonzalez, *et al.*, *Molecular Biology of the Cell* **29**, 2591 (2018).

19. M. Guo, *et al.*, *Proceedings of the National Academy of Sciences of the United States of America* **114**, E8618 (2017).

20. K. Xie, Y. Yang, H. Jiang, *Biophysical Journal* **114**, 675 (2018).

21. C. Tomba, V. Luchnikov, L. Barberi, C. Blanch-Mercader, A. Roux, *Developmental Cell* **57**, 1257 (2022).

22. T. H. Hui, *et al.*, *Physical Review Letters* **113**, 1 (2014).

23. J. Park, S. Jia, D. Salter, P. Bagnaninchi, C. G. Hansen, *The EMBO Journal* pp. 1–21 (2022).

24. S. Watkins, H. Sontheimer, *The Journal of neuroscience : the official journal of the Society for Neuroscience* **31**, 17250 (2011).

25. D. C. TOSTESON, J. F. HOFFMAN, *The Journal of general physiology* **44**, 169 (1960).

26. H. F. Cantiello, *The Journal of experimental zoology* **279**, 425 (1997).

27. J. H. Henson, *Microscopy Research and Technique* **47**, 155 (1999).

28. X. Li, D. Prins, M. Michalak, L. Fliegel, *American Journal of Physiology - Cell Physiology* **305**, 1161 (2013).

29. L. M. Sjøgaard-Frich, *et al.*, *eLife* **10** (2021).

30. L. He, *et al.*, *Journal of Cell Science* **131**, 1 (2018).

31. C. Cadart, *et al.*, *Methods in cell biology* **139**, 103 (2017).

32. N. Rochman, K. Yao, N. Perez Gonzalez, D. Wirtz, S. Sun, *BIO-PROTOCOL* **10** (2020).

33. A. S. Pivovarov, F. Calahorro, R. J. Walker, *Invertebrate Neuroscience* **19**, 1 (2019).

34. T. J. Jentsch, *Nature Reviews Molecular Cell Biology* **17**, 293 (2016).

35. Y. Li, X. Zhou, S. X. Sun, *Frontiers in Cell and Developmental Biology* **9**, 1 (2021).

36. T. L. Nagy, J. D. Strickland, O. D. Weiner, *bioRxiv* p. 2023.05.15.540704 (2023).

37. F. Guilak, G. R. Erickson, H. P. Ting-Beall, *Biophysical journal* **82**, 720 (2002).

38. T. Yeung, *et al.*, *Cell Motility and the Cytoskeleton* **60**, 24 (2005).

39. M. Ghibaudo, *et al.*, *Soft Matter* **4**, 1836 (2008).

40. S. Walcott, S. X. Sun, *Proceedings of the National Academy of Sciences of the United States of America* **107**, 7757 (2010).

41. A. Isomursu, *et al.*, *Nature Materials* **21** (2022).

42. J. M. Scholey, K. A. Taylor, J. Kendrick-Jones, *Nature* **287**, 233 (1980).

43. M. Uehata, *et al.*, *Nature* **389**, 990 (1997).

44. S. Sakurada, *et al.*, *Circulation research* **93**, 548 (2003).

45. T. Miyamoto, *et al.*, *Journal of Biological Chemistry* **289**, 16565 (2014).

46. S. M. Cahalan, *et al.*, *eLife* **4** (2015).

47. S. Yang, *et al.*, *Nature Communications* **13**, 7467 (2022).

48. M. Yao, *et al.*, *Science Advances* **8**, 1 (2022).

49. S. P. Denker, D. C. Huang, J. Orlowski, H. Furthmayr, D. L. Barber, *Molecular Cell* **6**, 1425 (2000).

50. S. Wakabayashi, T. Ikeda, T. Iwamoto, J. Pouysségur, M. Shigekawa, *Biochemistry* **36**, 12854 (1997).

51. P. Mistriotis, *et al.*, *Journal of Cell Biology* **218**, 4093 (2019).

52. A. J. Lomakin, *et al.*, *Science* **370** (2020).

53. V. Venturini, *et al.*, *Science* **370** (2020).

54. Y. Kalukula, A. D. Stephens, J. Lammerding, S. Gabriele, *Nature Reviews Molecular Cell Biology* **23**, 583 (2022).

55. J. Irianto, *et al.*, *Biophysical Journal* **104**, 759 (2013).

56. Y. Song, *et al.*, *Nature Materials* **21**, 1191 (2022).

57. A. Krämer, J. Green, J. Pollard, S. Tugendreich, *Bioinformatics* **30**, 523 (2014).

58. C. R. Boyd-Shiwarski, *et al.*, *Cell* **185**, 4488 (2022).

59. E. Zlotek-Zlotkiewicz, S. Monnier, G. Cappello, M. Le Berre, M. Piel, *Journal of Cell Biology* **211**, 765 (2015).

60. C. L. Yankaskas, *et al.*, *Nature Biomedical Engineering* **3**, 452 (2019).

61. A. Colom, *et al.*, *Nature Chemistry* **10**, 1118 (2018).

62. R. N. Palchesko, L. Zhang, Y. Sun, A. W. Feinberg, *PLoS ONE* **7**, e51499 (2012).

Acknowledgments

The We would like to thank Ikbal Choudhury, Shaozheng Sun, and Bin Sheng Wong for their helps in experiments and discussions. This work was supported in part by R01 GM134542 (to S.X.S. and K.K.) and NSF 2045715 (to Y.L.). G.S. and A.P.F acknowledge the support from Bloomberg Philanthropies. We also thank John Hopkins University Integrated Imaging Center for microscope support and Rockfish HPC for computational source.

Author Contributions

Q.N., K.K., and S.X.S conceptualized and designed the study. Q.N., Z.G., and J.F. conducted all live cell experiments and analyzed the data (with Y.Wu). Z.G. and J.F. fabricated all microfluidic devices and PDMS substrate. Y.Z. and S.X.S. developed the cell volume model and analyzed the simulation results (with Q.N.). Z.G., Y.Y., A.V. and Y.Wang generated and validated the CRISPR Piezo1-knockout cell line, and K.B. and A.S. generated and validated the shNHE1 cell lines. Q.N. and Z.G. conducted immunofluorescence and DNA methylation experiments. G.S. and A.P.F. performed the gene expression and IPA analysis for RNA-seq (with Q.N.). Q.N. and S.X.S. wrote the manuscript, and Z.G., Y.L., K.B., A.S., A.P.F., and K.K. edited the manuscript.

Supplementary Figures

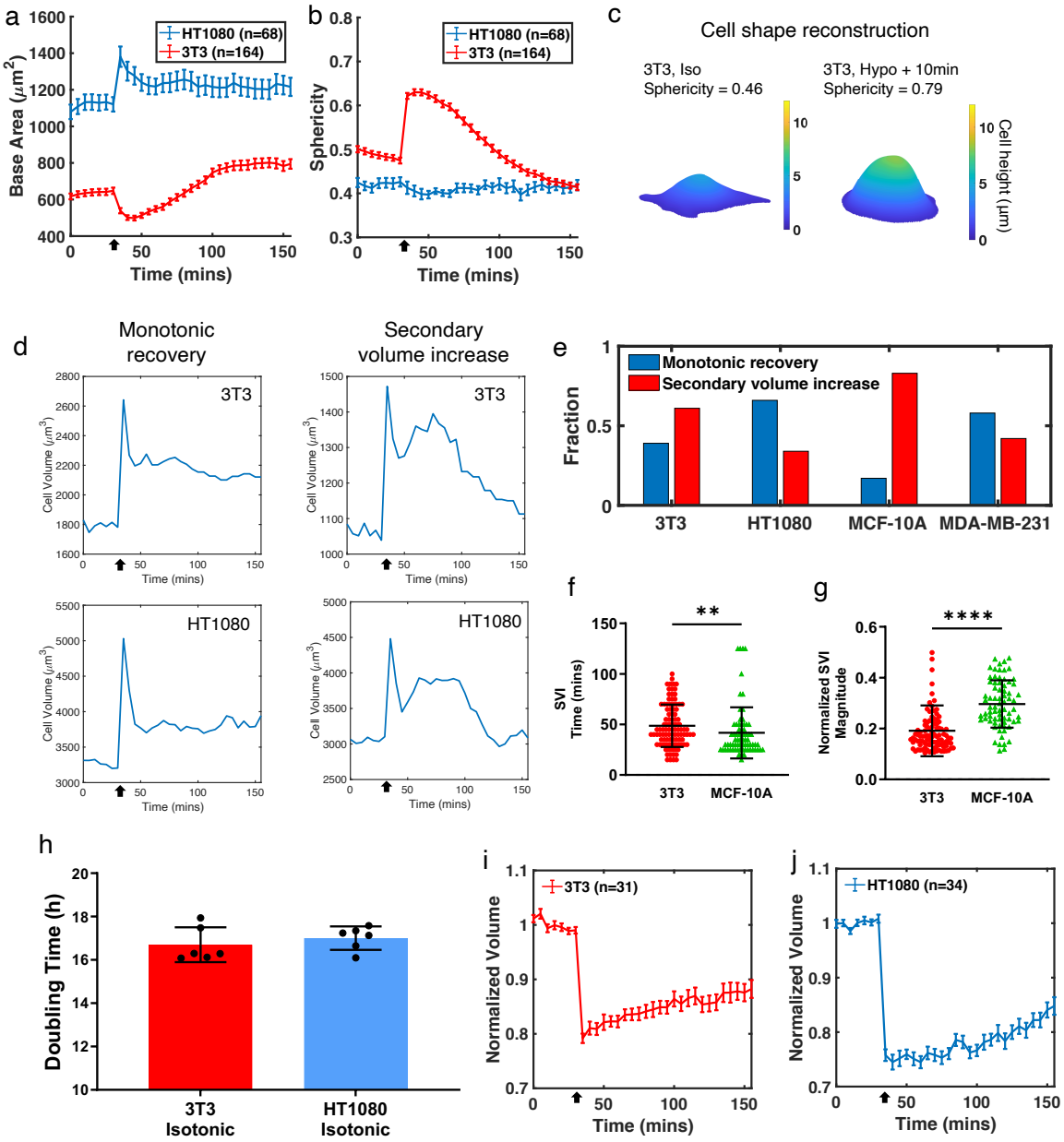

Figure S1: **Hypotonic shock induced cell area and shape changes, cell volume variation, double time, and volume changes under hypertonic shock.** (a) Cell base area dynamics with 50% hypotonic shock at 30mins. (b, c) Cell sphericity dynamics (b) with 50% hypotonic shock at 30mins. Sphericity is calculated as $\frac{\pi^{\frac{1}{3}}(6V)^{\frac{2}{3}}}{A_{surface}}$. Surface area $A_{surface}$ is calculated from cell shape reconstruction based on FXm (c). (d) Representative single cell volume *versus* time after hypotonic shock. (e) The fraction of cells showing monotonic recovery and SVI. The SVI cell type is defined as cell showing at least 10% volume increase after initial recovery. (f, g) The time (f) and magnitude (g) of the SVI. (h) The doubling time of 3T3 and HT1080 in isotonic media, respectively. N = 6 for all conditions. (i, j) 3T3 (i) and HT1080 (hj volume dynamics with 50% hypotonic shock at 30mins. (a, b, i, j) Error bars indicates standard error of mean (SEM). (f, g) Error bars indicates standard deviation. Mann-Whitney U tests were conducted. ****p<0.0001, ***p<0.001, **p<0.01, and ns p>0.05.

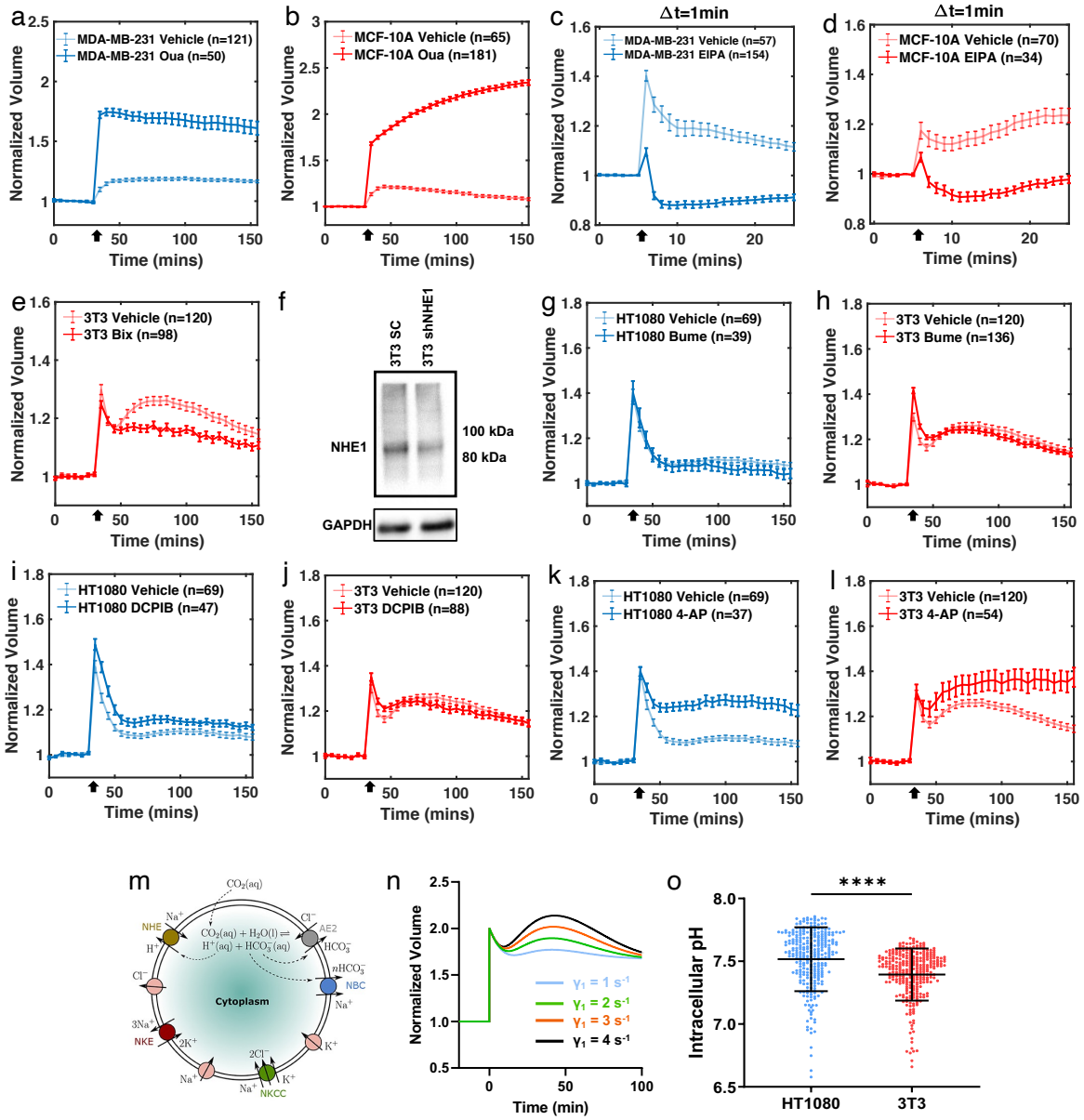

Figure S2: **The effects of Na^+-K^+ flux in regulating cell volume.** (a, b) MDA-MB-231 (a) and Mcf-10a (b) volume dynamics under Ouabain treatment. (c, d) MDA-MB-231 (c) and Mcf-10a (d) volume dynamics under EIPA with hypotonic shock applied at 5 mins. Frame rate is 1 min. (e) 3T3 volume dynamics under Bix with hypotonic shock applied at 30 mins. (f) Representative western blot from 3T3 transduced with shRNA sequences to NHE1 or a noncoding scramble control (SC) sequence. (g-l) 3T3 and HT1080 volume dynamics under Bume (g for HT1080, h for 3T3), DCPIB (i for HT1080, j for 3T3), or 4-AP treatment (k for HT1080, l for 3T3). (m) A cartoon illustration showing the main ion transportation of the cell volume model. (n) Simulated 3T3 volume dynamics with different NHE activation functions. (o) Intracellular pH of HT1080 and 3T3 at homeostasis. (a-e, g-i) Error bars indicate SEM. (o) n = 291 and 206, respectively. Error bars indicate standard deviation. Mann-Whitney U tests.

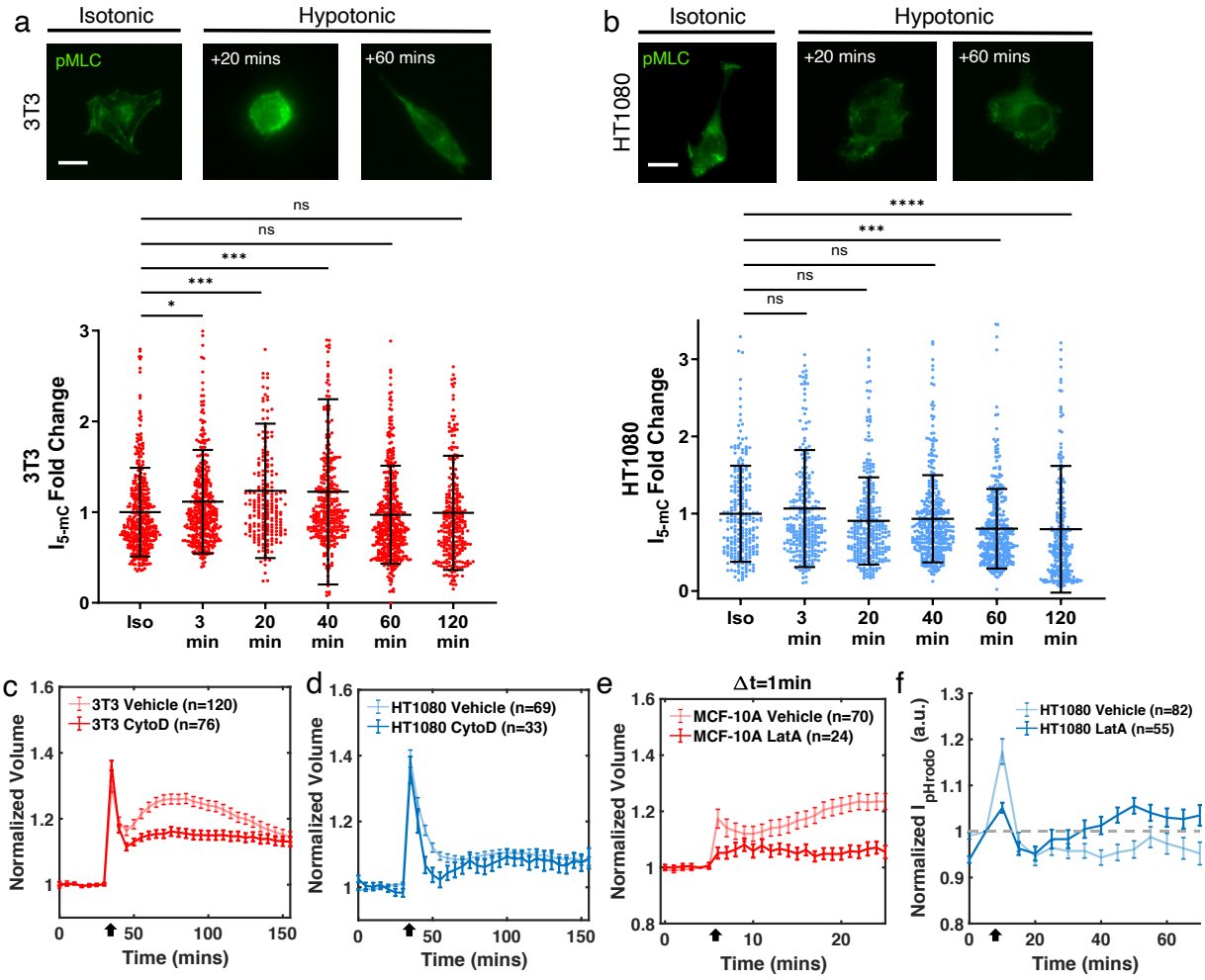

Figure S3: **Hypotonic shock induces changes in pohospho-myosin light chain activity and volume dynamics under actomyosin disruption.** (a, b) The representative immunofluorescent images of pohospho-myosin light chain and the quantifications of 3T3(a) and HT1080 (b). Cells were fixed in isotonic meida, and 3, 20, 40, 60 and 120 minutes after hypotonic shock. (c, d) 3T3 (c) and HT1080 (d) volume dynamics under CytoD treatment with hypotonic shock applied at 30 mins. (e) MCF-10A volume dynamics under LatA treatment with hypotonic shock applied at 5 mins. Frame rate = 1min. (f)Intensity of pHrodo-red AM during hypotonic shock for HT1080 vehicle control and under LatA treatment. (a, b) For 3T3 (a), n = 405, 401, 216, 330, 441, 287. For HT1080 (b), n = 224, 283, 296, 358, 366, 284. Error bars indicate standard deviation. Kruskal–Wallis tests followed by Dunn's multiple-comparison test. (c-f) Error bars indicate SEM. (a, b) Scale bars, 20 µm.

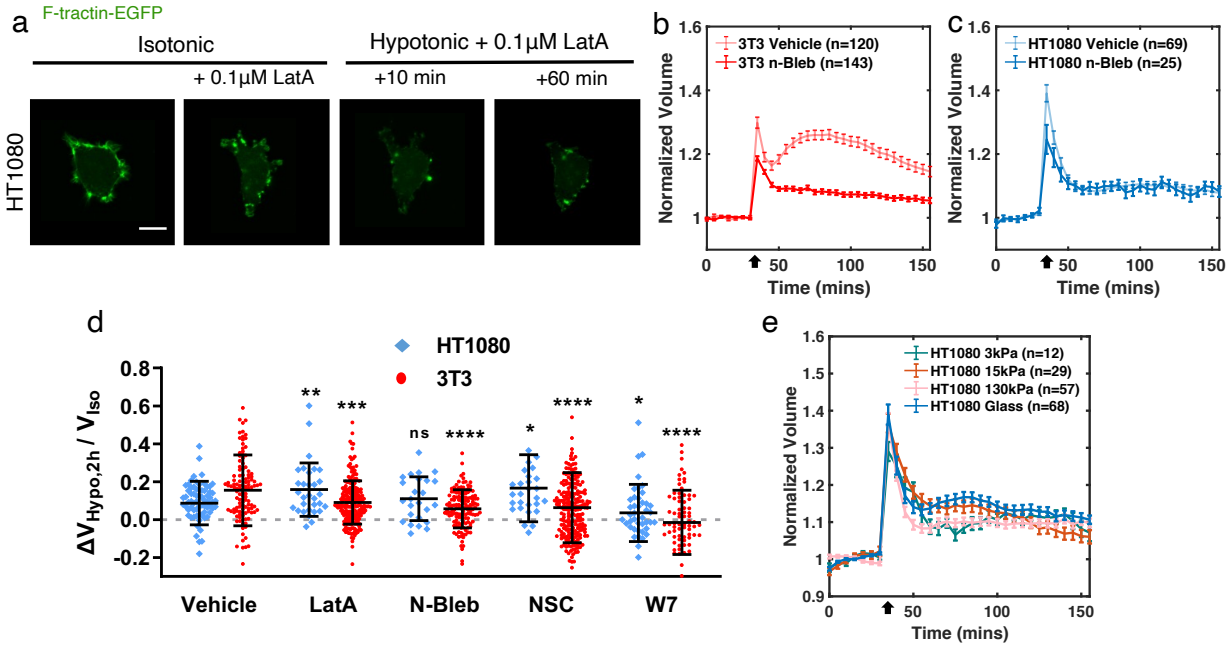

Figure S4: **3T3 and HT1080 volume and actin dynamics change under actomyosin disruption or grown on varied substrate stiffness and hypotonic shock.** (a) Confocal images of EGFP-F-tractin transfected HT1080 subjected to LatA treatment before and after hypotonic shock. (b, c) 3T3 (b) and HT1080 (c) volume dynamics under n-Bleb treatment with hypotonic shock applied at 30 mins. (d) Relative cell volume change 2 hours after applying hypotonic shock under drug disruption of cytoskeleton. (e) HT1080 volume dynamics under hypotonic shock on 3, 15, and 130 kPa PDMS substrate and on glass. (b, c, e) Error bars indicate SEM. (d) Error bars indicate standard deviation. Kruskal–Wallis tests followed by Dunn's multiple-comparison were conducted between data sets and the vehicle control of the corresponding cell type. $n^{HT1080}_{Vehicle} = 69, n^{3T3}_{Vehicle} = 120, n^{HT1080}_{LatA} = 31, n^{3T3}_{LatA} = 212, n^{HT1080}_{n-Bleb} = 25, n^{3T3}_{n-Bleb} = 143, n^{HT1080}_{W7} = 43, n^{3T3}_{W7} = 77, n^{HT1080}_{NSC} = 28, n^{3T3}_{NSC} = 222$. (a) Scale bar, 20 μm.

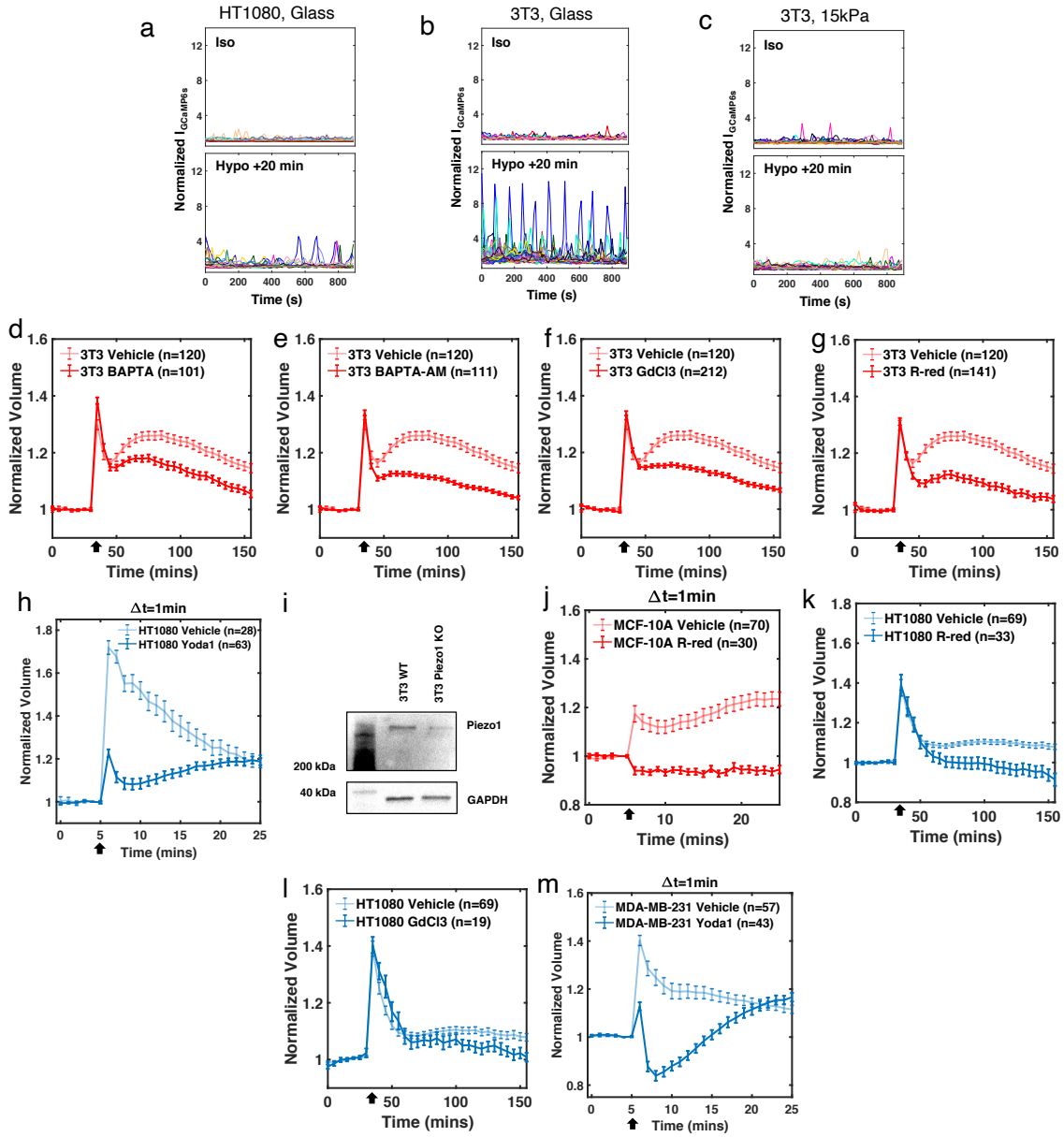

Figure S5: **Ca^{2+} signaling affects cell volume regulation.** (a-c) Single-cell GCaMP6s dynamics in isotonic media (upper) and 20 minutes after hypotonic shock (lower) for HT1080 on glass (a), 3T3 on glass (b), and 3T3 on 15 kPa (c). Imaged at 10-second frame rate. (d-g) 3T3 volume dynamics under BAPTA (d), BAPTA-AM (e), $GdCl_3$ (f), or Ruthenium-red (g). Hypotonic shock was applied at 30 mins. (h) HT1080 volume dynamics under Yoda1 treatment. Yoda1 was added together with hypotonic solution at 5 mins. (i) Representative western blot from 3T3 WT and Piezo1 CRISPR knockout cells. (j) MCF-10A volume dynamics under R-red treatment with hypotonic shock applied at 5 mins. Frame rate is 1 min. (k-l) HT1080 volume dynamics under R-red (k) or $GdCl_3$ (l) treatment with hypotonic shock applied at 30 mins. (m) MDA-MB-231 volume dynamics under Yoda1 treatment and hypotonic shock. Yoda1 and hypotonic shock were applied together at 5 mins. (a, d-h, j-m) Error bars indicate SEM.

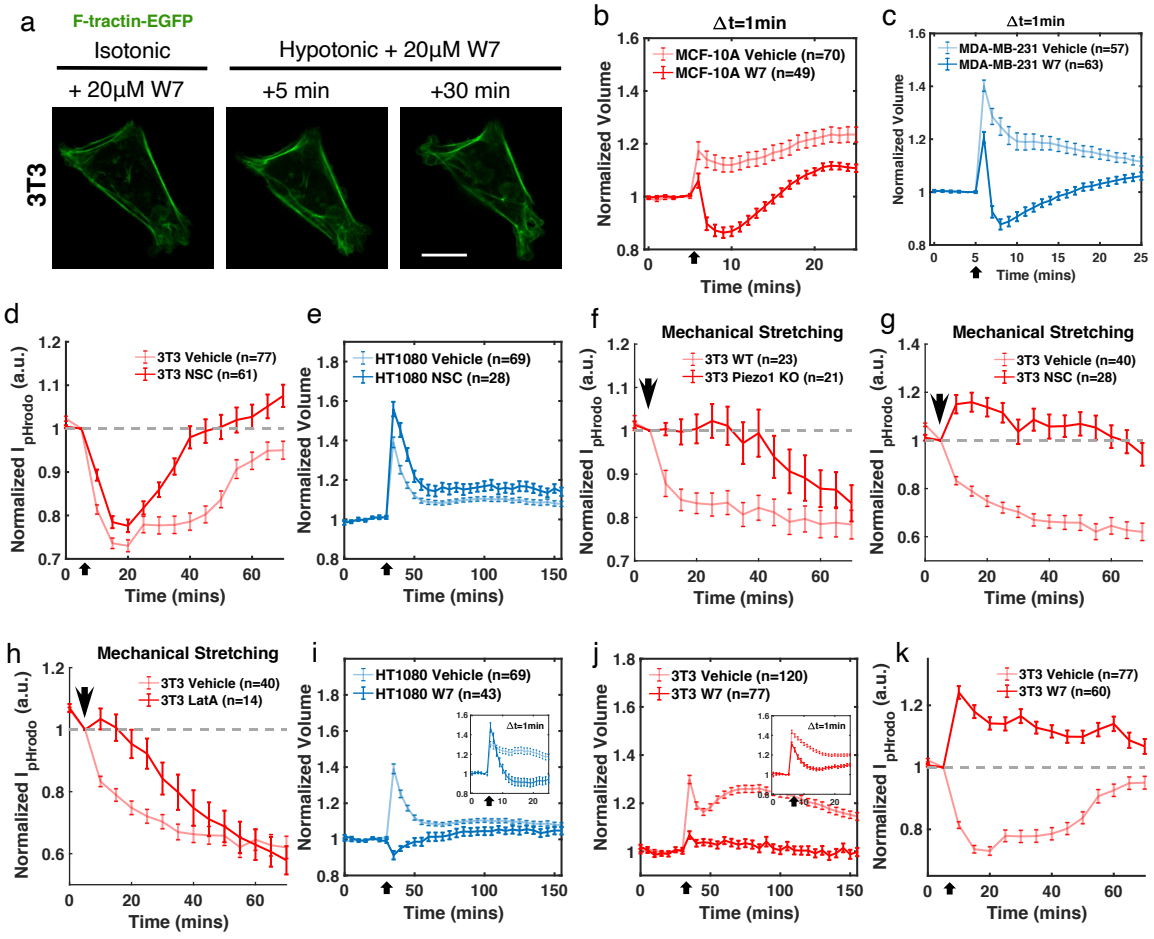

Figure S6: **Ca^{2+}, calmodulin and ezrin affect cell volume regulation.** (a) 3T3 expressing F-tractin with W7 treatment before and after hypotonic shock. Scale bar, 20 μm. (b-c) MCF-10A (b) and MDA-MB-231 (c) volume dynamics under W7 with hypotonic shock applied at 5 mins. (d) Intensity of pHrodo-red AM for 3T3 under NSC treatment and vehicle control. Hypotonic shock was applied at 5 mins. (e) HT1080 volume dynamics with NSC treatment and hypotonic shock applied at 30 mins. (f-g) pHrodo-red AM intensity of 3T3 WT and Piezo1 KO (f), 3T3 under NSC treatment (g) or under LatA treatment (h) with 20% uniaxial mechanical stretch. The mechanical stretch was applied at 5 mins, as indicated by the black arrow. (i-j) HT1080 (i) and 3T3 (j) volume dynamics under W7 treatment and hypotonic shock. The insert has 1 min frame rate (HT1080 Vehicle n = 53, W7 = 20, 3T3 Vehicle n = 42, W7 n = 46). (k) Intensity of pHrodo-red AM for 3T3 under W7 treatment and vehicle control. Hypotonic shock was applied at 5 mins. (b-k) Error bars indicate SEM. (a) Scale bar, 20 μm/

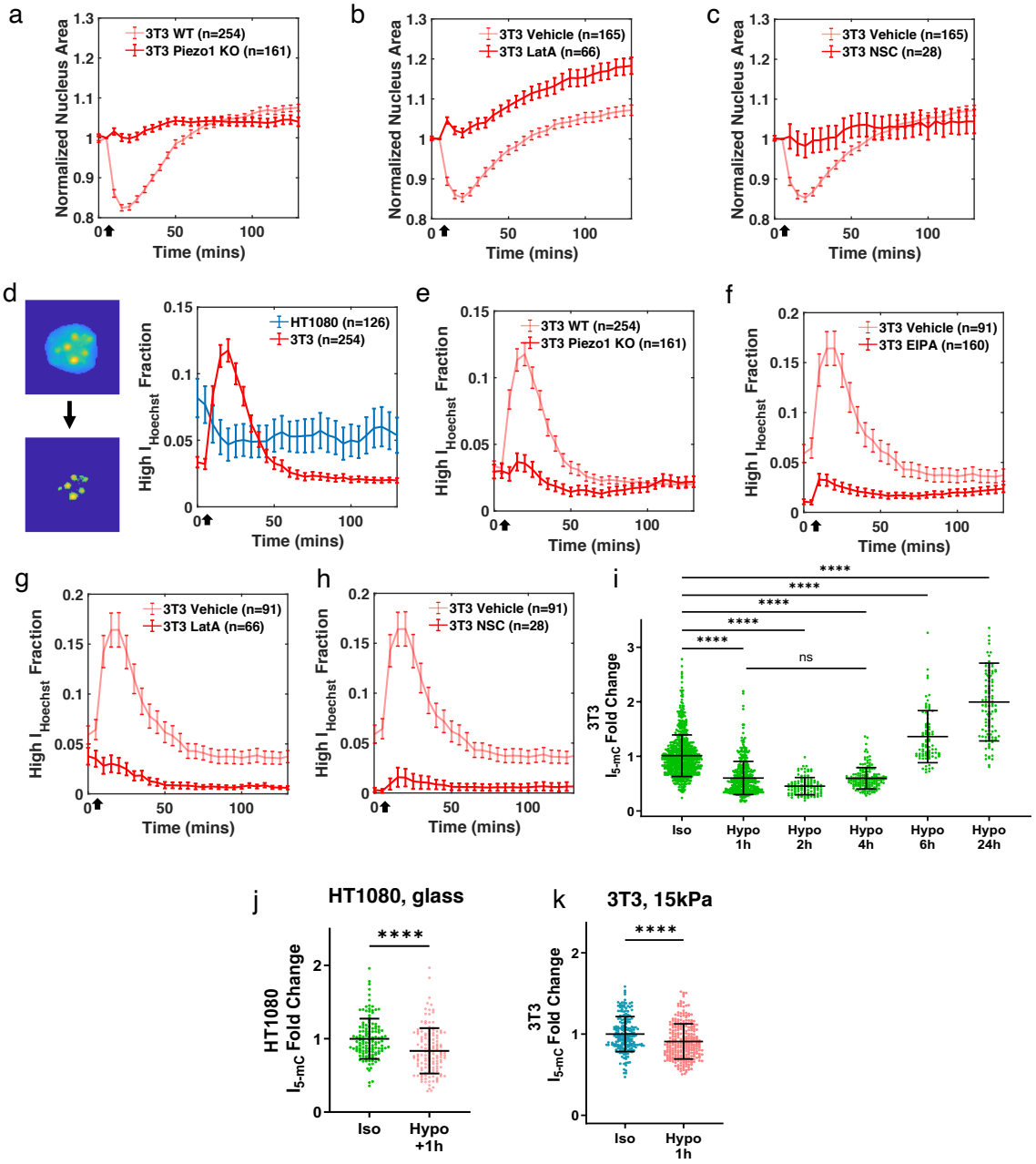

Figure S7: **Cytoskeletal activation of NHE1 triggers nucleus deformation and chromatin reorganization.** (a) Normalized nucleus area of 3T3 WT *versus* Piezo1 KO with hypotonic shock applied at 5 min. (b, c) Normalized nucleus area of 3T3 treated with LatA (b) or NSC (c). Hypotonic shock was applied at 5 min. (d) Fraction of 3T3 *versus* HT1080 nucleus regions expressing high Hoechst intensity, and a representative image analysis. Hypotonic shock applied at 5 min. (e) Fraction of 3T3 WT *versus* Piezo1 KO nucleus regions expressing high Hoechst intensity. (f-h) Fraction of 3T3 nucleus regions expressing high Hoechst intensity treated with EIPA, LatA, and NSC. (i) 3T3 5-mC expression fold change at different timepoints after hypotonic shock. (j, k) 5-mC expression fold changes of HT1080 on glass and 3T3 on 15 kPa PDMS substrate in isotonic condition *versus* exposing to hypotonic environment for 1 h. (a-h) Error bars indicate SEM. (i-k) Error bars indicate standard deviation. (i) Kruskal–Wallis tests followed by Dunn's multiple-comparison test. (j, k) Mann–Whitney U test.

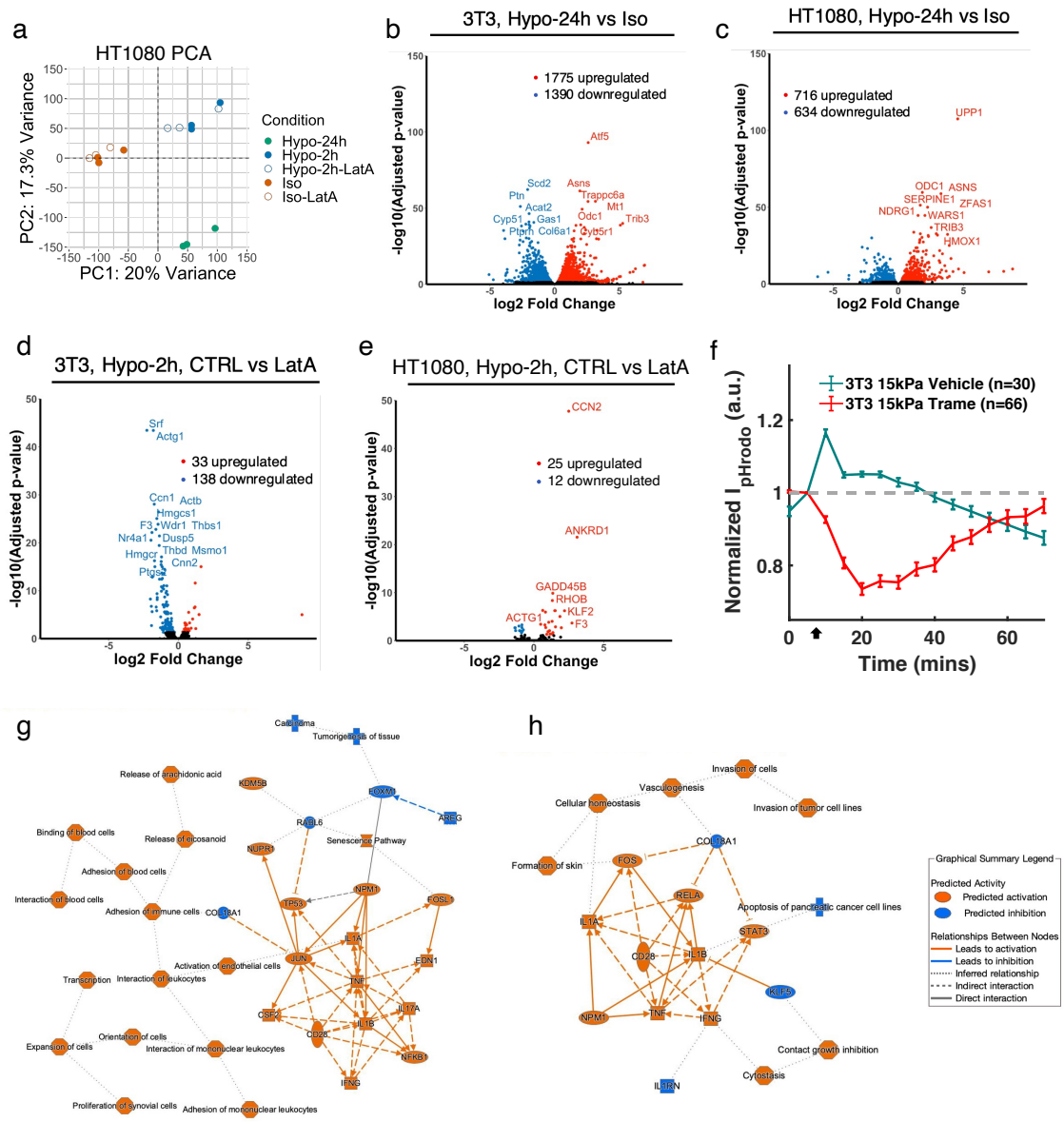

Figure S8: **Hypotonic shock induces transcriptomic changes.** (a) Principle component analysis (PCA) for HT1080 before and after hypotonic shock and with or without LatA treatment. N = 3 biological repeats. (b, c) Volcano plots showing differentially expressed genes (DEGs) at 24-hour hypotonic shock versus in isotonic media for 3T3 (b) and HT1080 (c). (d, e) Volcano plots showing DEGs at 2-hour hypotonic shock control versus LatA treatment for 3T3 (d) and HT1080 (e). (f) Intensity of pHrodo-red AM for 3T3 under Trametinib (Trame) treatment and vehicle control. Hypotonic shock was applied at 5 mins. (g, h) Summaries of pathways under 2-hour hypotonic shock for 3T3 (g) and HT1080 (h). (f) Error bars indicate SEM.
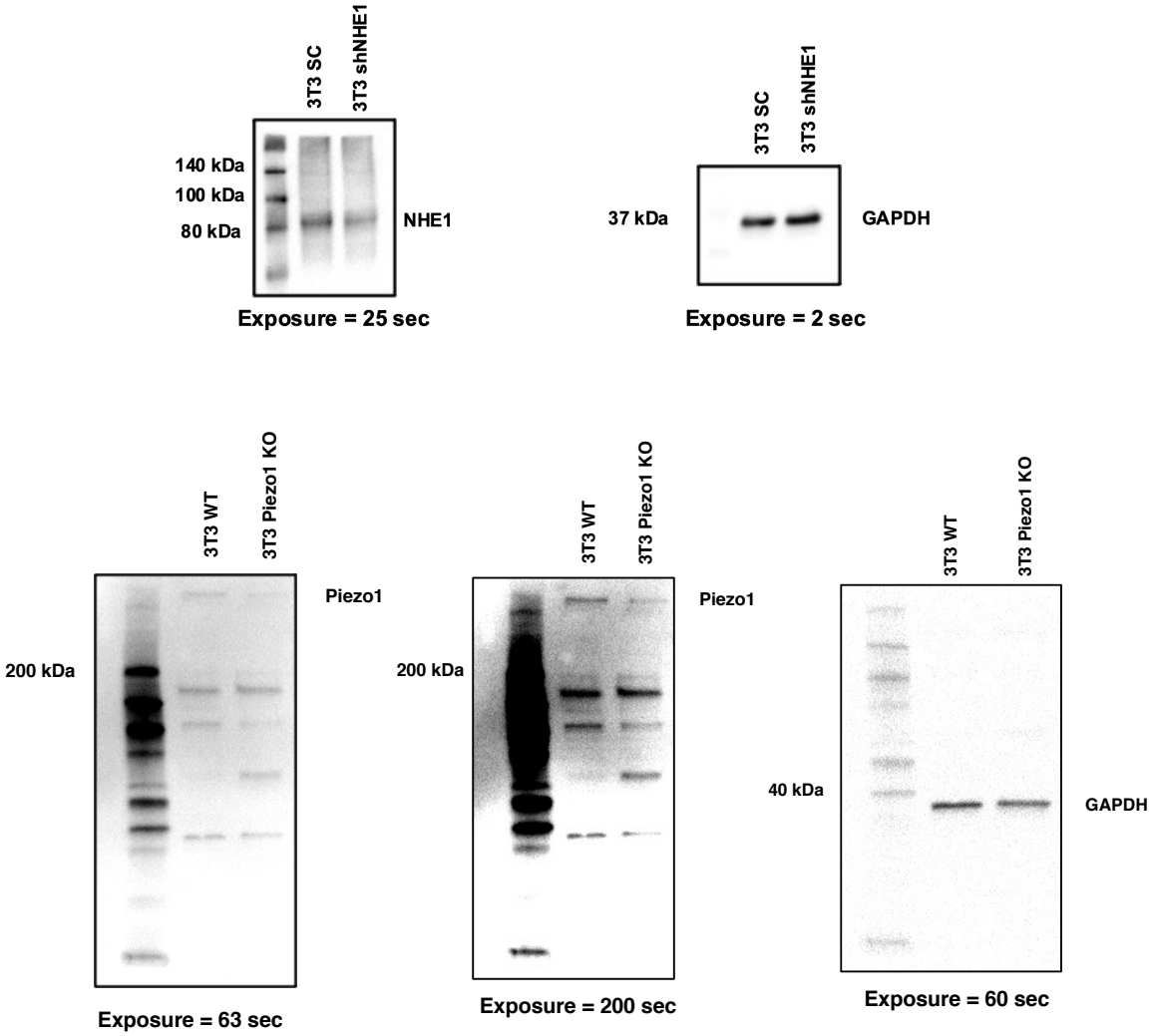
Uncropped western blot